

Research paper

Seismic characterisation of fault damage in 3D using mechanical and seismic modelling

Charlotte Botter ^{a,*}, Nestor Cardozo ^a, Stuart Hardy ^b, Isabelle Lecomte ^{c,1}, Gaynor Paton ^d, Alejandro Escalona ^a^a Department of Petroleum Engineering, University of Stavanger, 4036, Stavanger, Norway^b Institució Catalana de Recerca i Estudis Avançats (ICREA), Catalonia, Spain^c NORSAR, Gunnar Randers vei 15, 2007, Kjeller, Norway^d GeoTeric, Newcastle upon Tyne, NE1 2LA, United Kingdom

ARTICLE INFO

Article history:

Received 29 January 2016

Received in revised form

26 July 2016

Accepted 1 August 2016

Available online 3 August 2016

Keywords:

Seismic

Fault damage

Discrete element modelling

Ray-based seismic modelling

PSDM

Seismic attributes

ABSTRACT

Although typically interpreted as 2D surfaces, faults are 3D narrow zones of highly and heterogeneously deformed rocks with petrophysical properties differing from the host rock. Fault zones have been extensively studied in outcrop, but in the subsurface they are barely explored, mainly because they are at the limit of seismic resolution and are rarely drilled and cored. We present a 3D synthetic workflow to assess the potential of seismic data for imaging and characterising fault damage and properties. The workflow is based on forward modelling techniques. First, we run a 3D discrete element model to simulate faulting and associated deformation. Then, we use simple relationships to modify the initial elastic properties of the model based on its volumetric strain. From this reflectivity cube, we apply a ray-based, pre-stack depth migration simulator. Finally, from the resultant seismic image, we use seismic attributes to characterise the fault volume. We illustrate the workflow for a large displacement normal fault in a sandstone-shale sequence for two cases, one with constant fault displacement and another with linearly variable displacement along strike. Seismic cubes of these models for a homogeneous overburden and several wave frequencies are generated. High frequencies show the impact of the fault on the offset and folding of the reflectors. In the variable fault slip model, the fault has less impact as the displacement decreases, and the fault tipline can be interpreted. We extract the fault geobody using three combined seismic attributes: dip, semblance and tensor. The geobody for the constant fault displacement model corresponds to an inner high-deformation area within the fault zone, while in the variable fault slip model the geobody captures better the entire fault zone. Cross plotting of amplitudes and strains shows that the geobody contains all range of strains, but almost all high strain values are within the geobody. This allows a direct comparison between the fault zone identified on the seismic image and that in the mechanical model.

© 2016 Elsevier Ltd. All rights reserved.

1. Introduction

Although normally interpreted as 2D surfaces in seismic, faults are 3D narrow zones of highly and heterogeneously deformed rocks with petrophysical properties differing from the host rock

(Faulkner et al., 2010 and references therein). Faults directly impact reservoir connectivity and their 3D structure and properties are primary controls on fluid flow. Fault internal structure, however, is difficult to image in seismic because it is often at the limit of seismic resolution (Townsend et al., 1998; Dutzer et al., 2010; Long and Imber, 2011). Faults have high variability in 3D, and specific combinations of lithology, fault displacement and fault related deformation result in different seismic signature, which prevents any generalisation. We lack tools to predict fault variability and correctly represent faults in reservoir models (Manzocchi et al., 2010).

3D fault architecture is hardly taken into account during seismic interpretation. Most seismic interpretation studies target the

* Corresponding author.

E-mail addresses: charlotte.botter@gmail.com, charlotte.botter@uis.no (C. Botter), nestor.cardozo@uis.no (N. Cardozo), stuart.hardy@icrea.cat (S. Hardy), isabelle.lecomte@norsar.com (I. Lecomte), gaynor.paton@geoteric.com (G. Paton), alejandros.escalona@uis.no (A. Escalona).

¹ New affiliation: University of Bergen, Realfagbygget, Allégt. 41, Postboks 7803, 5020, Bergen, Norway. Isabelle.lecomte@uib.no.

recognition of fault networks. Few studies investigate the potential of seismic data to characterise fault zone architecture and properties. [Townsend et al. \(1998\)](#) use seismic amplitude anomalies to detect small scale faulting. [Cohen et al. \(2006\)](#) transform seismic data using a coherence attribute for automatic extraction of fault surfaces. [Dutzer et al. \(2010\)](#) use volume attributes to determine fault internal structure and transmissibility. [Long and Imber \(2010\)](#) analyse fault related deformation using an apparent dip attribute. [Hale \(2013\)](#) estimates fault throws on extracted fault surfaces using image-processing methods. [Botter et al. \(2014\)](#) look at the response of seismic amplitude to normal faulting in 2D synthetic seismic models. [Iacopini et al. \(2016\)](#) use seismic attributes and image-processing methods to determine “seismic facies” within fault zones. These studies highlight the potential of seismic for fault structure and property interpretation.

Attributes such as azimuth, dip, curvature, semblance, tensor and eigenstructures, or structurally oriented filters, can be used to enhance fault detection and interpretation (e.g. [Bahorich and Farmer, 1995](#); [Gersztenkorn and Marfurt, 1999](#); [Chopra et al., 2000](#); [Jackson and Kane, 2012](#)). Seismic expression of faults, however, varies considerably even within the same seismic cube, which leads to the use of workflows consisting of several attributes in order to get optimum results. [Dutzer et al. \(2010\)](#) divide the fault zone into inner and outer zones, and use semblance, dip and tensor attributes for the inner zone, and structurally oriented curvature for the outer zone. They evaluate lateral thickness and changes in one selected seismic attribute response. This workflow leads to a better mapping of fault damage zones including those at the limit of seismic resolution. [Iacopini and Butler \(2011\)](#) and [Iacopini et al. \(2012\)](#) present a visualisation workflow for deep-water fold and thrust belts. They use opacity, structurally oriented filters and volume attributes such as semblance, curvature and spectral decomposition, together with visualisation methods such as volume rendering and blending techniques to improve image quality of thrusts and their associated deformation from post-stack seismic data. [Iacopini et al. \(2016\)](#) resolve the seismic expression of fault damage by combining tensor, semblance and instantaneous phase attributes. Using image analysis techniques and cross-plots of seismic attributes, they discriminate the seismic expression of fault damage from seismic noise and define unsupervised seismic facies from the fault zone.

Working with 3D seismic data is challenging. For typical depths of investigation of 2–4 km, seismic will hardly capture vertical features less than 12–25 m. Horizontal resolution in migrated seismic data is highly dependent on many factors, including noise, and it is mostly lower or at best equal to vertical resolution. Horizontal uncertainties are higher than vertical uncertainties, often by a factor of 2 ([Sheriff and Geldart, 1995](#)). Thin beds and fault zones can therefore interfere and not be well represented in seismic images. Noise is often present in seismic data, due to the acquisition techniques and the complex 3D structures encountered. Moreover, when the seismic data are handed to the interpreter, several processing steps have been applied, which might have influenced the final seismic image. All these factors have to be taken into consideration in order to obtain a correct representation of the faults and their associated deformation. The interpreter will combine cross-lines, in-lines and time slices to extract fault architecture using the offset and distortion (e.g. departure from regional dip) of reflector surfaces. Display and seismic attributes will help to enhance structural details. However, this is a laborious and highly subjective process. On the other hand, one may use automated software-based techniques to analyse and compare each seismic trace throughout the complete seismic volume, and ultimately display and extract the fault volume in 3D ([Cohen et al., 2006](#); [Dutzer et al., 2010](#); [Iacopini and Butler, 2011](#); [Iacopini et al., 2012](#),

[2016](#); [Hale, 2013](#)). However, one cannot fully rely on these techniques. An independent evaluation on the influence of all involved parameters is needed to fine-tune the mapping and obtain an accurate and realistic fault zone structure.

Besides obtaining a fault damage volume, the ultimate purpose of seismic fault characterisation is to retrieve the rock properties associated to the fault zones and their relative variation with respect to those of the host rock. Can the seismic data provide enough information to do this? A common approach is to tie the seismic with well data in order to associate a specific seismic response to a range of rock properties. However, well drillers avoid faults and coring of fault zones is very rare. Several studies combine well and core data with seismic in order to improve the subsurface interpretation of faults. [Hesthammer and Fossen \(1997\)](#) combine attributes analyses on seismic data to the many well log and core data available in the Gullfaks field area to separate fault features from coherent noise. Faults with a throw of a meter-scale that can be identified in core data are also visible on well log correlation because of a scarce amount of fractures outside of the fault zones. [Aarland and Skjerven \(1998\)](#) describe an exceptional case combining seismic and core data to characterise a fault zone in the North Sea. They observe that fault zone thickness is controlled by parameters such as lithology and stress fields. [Koledoye et al. \(2003\)](#) apply a conceptual model to decompose the seismic expression of a large resolvable normal fault into segments to quantify shale smearing between each segment, and the use of well log data makes it possible to identify shale layers less than 10 m thick. [Færseth et al. \(2007\)](#) present some examples of fault seal prediction combining seismic data and fault cores from the North Sea to determine fault architecture and shale smearing. While these studies highlight the necessity of combining well log and core data with seismic in order to interpret features below seismic resolution, we cannot generalise or entirely predict fault sealing from these particular, relatively few cases.

The main purpose of this paper is to describe a synthetic workflow for the characterisation of faults and their related deformation as volumes in 3D seismic data ([Fig. 1](#)). This workflow is based on 3D geomechanical modelling of faulting using a discrete element method (DEM; e.g. [Carmona et al., 2010](#), [Fig. 1a](#)), simple relationships to modify the model's initial acoustic properties according to finite strain ([Botter et al., 2014](#), [Fig. 1b](#)), a ray-based pre-stack depth migration (PSDM) simulator ([Lecomte, 2008](#); [Lecomte et al., 2015](#), [Fig. 1c](#)), and a fault volume characterisation technique based on seismic attributes (e.g. [Cohen et al., 2006](#); [Chopra and Marfurt, 2007](#); [Iacopini and Butler, 2011](#); [Iacopini et al., 2012](#), [2016](#); [Hale, 2013](#), [Fig. 1d](#) and [e](#)). This is a continuation of our work in 2D ([Botter et al., 2014](#)), now implemented in 3D, with the additional use of seismic attributes to extract the fault zone volumes ([Fig. 1d](#)). Since the fault geometry and finite strain are known in the mechanical model, we can use the workflow to evaluate the performance of the seismic attributes analysis to image the fault zone and its internal structure ([Fig. 1e](#)). We apply the workflow to a 3D large displacement (100 m throw) normal fault in an interlayered sandstone-shale sequence for two situations, one with constant fault displacement and another with linearly variable displacement along strike. The second model allows us to study the variation of fault structure along strike and the performance of seismic on defining the fault tipline. Fault zones in extensional settings have a large range of geometries and associated fault damage. In this paper, we target fault damage that can be observed on seismic data, therefore at scale above seismic resolution. The fault models obtained with our DEM are at seismic scale and reservoir depths conditions, but they are also subjected to computing restrictions that limit the minimum size of particles and result in a large width of the fault zone. Therefore, the models

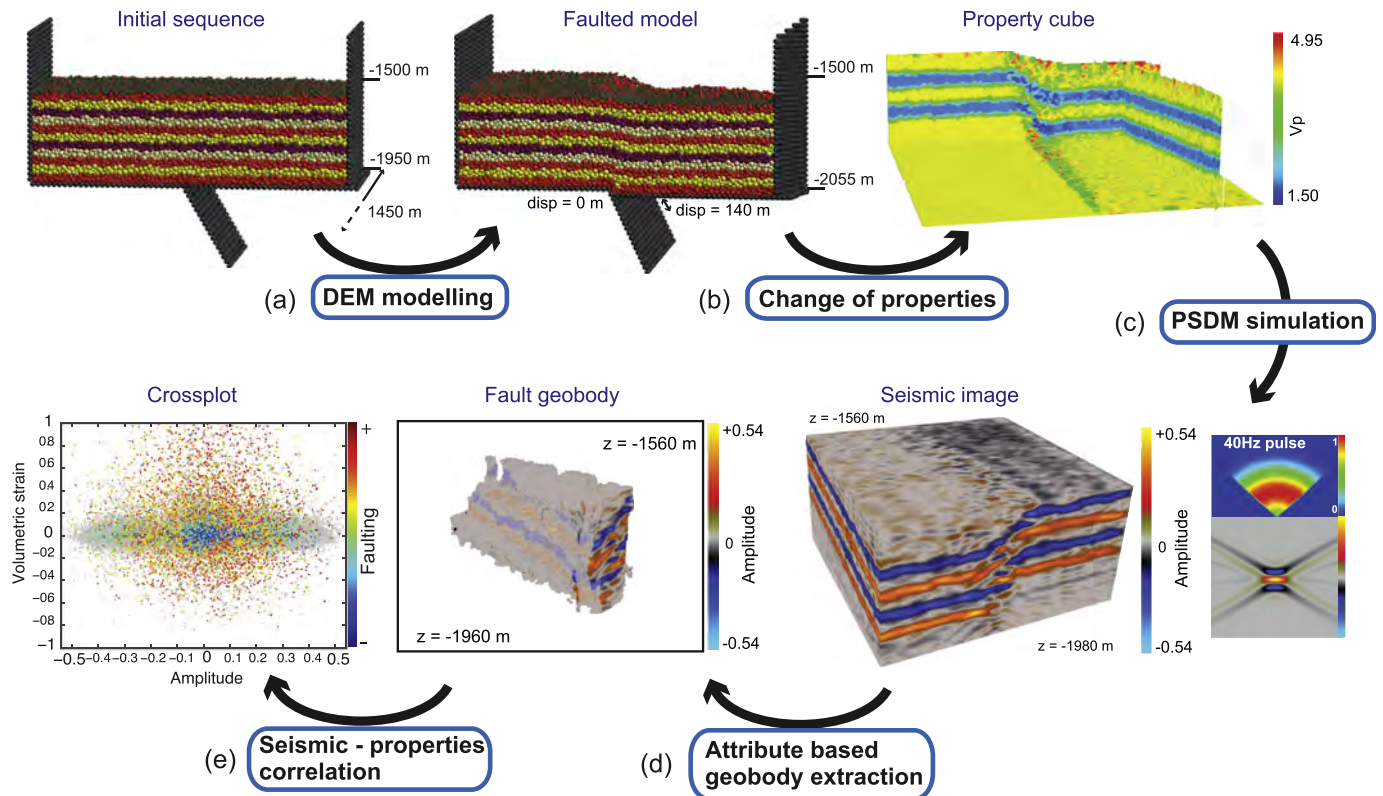


Fig. 1. Workflow of this study: (a) DEM modelling, (b) Change of elastic properties due to volumetric strain in DEM, (c) PSDM simulation on reflectivity grid, (d) Attribute-based geobody extraction, and (e) Correlation between seismic amplitude and finite strain.

simulate mainly fault-propagation folding (e.g., [Withjack et al., 1990](#); [Ferrill et al., 2005, 2007](#); [Lewis et al., 2015](#)), with a maximum fault throw at the base of the model and a wider fault zone and associated folding towards the top ([Fig. 1b](#)). Overall, our methodology provides better ways to understand the impact of faulting and fault damage on seismic, which leads to the development of better methods for seismic characterisation of faults.

2. Methodology

Our methodology is divided in two steps: 1. Forward modelling, consisting of DEM mechanical modelling, change of acoustic properties due to finite strain, and seismic modelling ([Fig. 1a–c](#)), and 2. Seismic-attribute based identification and interpretation ([Fig. 1d–e](#)).

2.1. Modelling techniques

2.1.1. Mechanical modelling

The DEM is a discontinuum method used to simulate the dynamic evolution of a system of discrete elements or particles under applied forces and displacement boundary conditions. As any modelling technique, the DEM presents advantages and disadvantages for its application to geological problems ([Gray et al., 2014](#)). The main advantage is that the method is capable of realistically and naturally model large deformations, fracturing, and fault development. The disadvantage is that because of computational limitations, which restrict the number of particles in the model, particles sizes in km scale simulations are in the order of meters, which prevents this large size models to capture the intricate mechanics at the granular scale. In addition, there are no rules for relating the particle properties to the bulk behaviour of the particle

assemblage, such that a trial and error calibration is needed. One may believe that a model that replicates bulk behaviour, but not the physics at the smaller granular scale is not useful (it is certainly not correct). However, the same line of reasoning would render scale models such as sandbox experiments useless. Like the grains in a meter size sandbox experiment of km size faulting do not represent the grains of the sedimentary rocks being modelled, nor do the particles of the DEM represent sedimentary grains. Both the scale sandbox experiment and the DEM intend to simulate bulk, at the smallest, meter scale strain. It is within this context that we use the DEM and its results.

The specific DEM formulation used here is based on the lattice solid model of [Mora and Place \(1993\)](#), further developed by [Hardy and Finch \(2005, 2006\)](#), and [Hardy et al. \(2009\)](#). The rock mass is treated as an assemblage of spherical particles in 3D ([Fig. 2a](#)). These particles have a given radius and density. They interact with elastic, frictional and gravitational forces. Faulting is induced by a displacement discontinuity at the base of the model, which induces faulting and folding of the sequence above ([Fig. 2b](#)). This kind of deformation is common in extensional fault systems (possibly at their early stage), where synthetic layer dips ([Ferrill et al., 2005](#)) or strong dip gradients ([Long and Imber, 2010](#)) adjacent to the faults are observed. Similar 2D DEM simulations have been previously run at small or large scales. [Abe et al. \(2011\)](#) looked at the formation of normal faults in a brittle-cohesive material above a basement fault for cm-scale models using bonded particles. Particle packing, location and style of faulting, and cohesion control the development of the faults. [Finch et al. \(2004\)](#) used a DEM with bonded particles for modelling extensional fault-propagation folding above rigid basement fault blocks in multilayer sequences at km-scale. The monocline and zone of deformation widths are controlled by the fault dip, the competence, and layered anisotropy of the rock

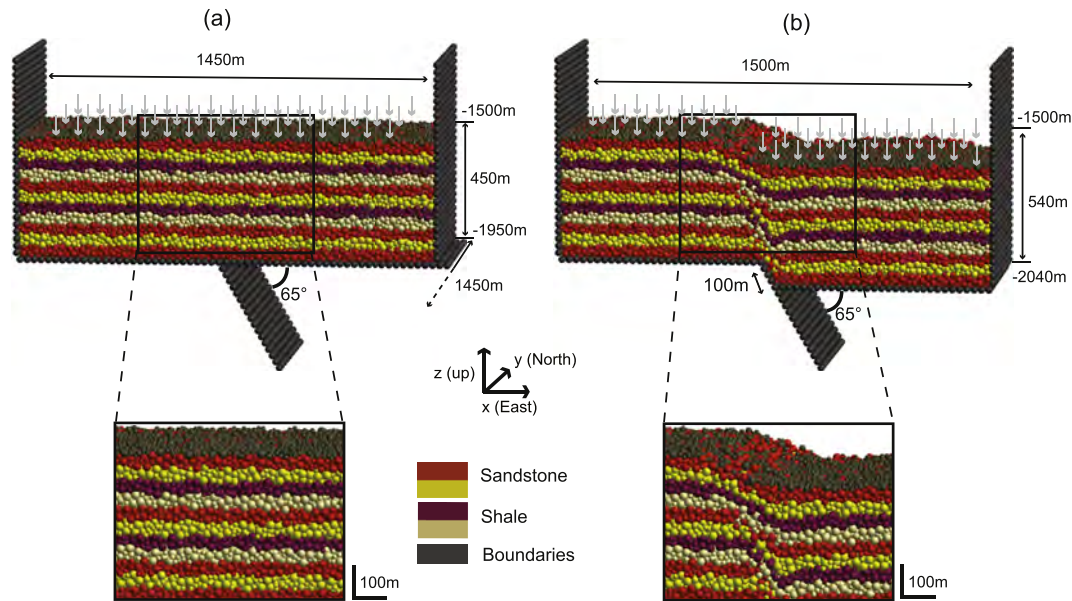


Fig. 2. 3D DEM models. (a) Initial assemblage before deformation, the grey arrows are the overburden tractions. (b) The model after 100 m fault displacement. Close up shows the redistribution of the overburden particles.

material. Schöpfer et al. (2007) looked at the growth of normal faults in multilayers m-scale sequences, using layers of bonded and unbonded particles to represent different competence of the layers. They observed changes of fault dip due to the strength (both tensile and compressive) of the layers, and that the fault width increases with fault displacement. Our DEM generates a realistic distribution of fault damage, including a wide fault zone and forced folding above a breaching fault in the deepest part of the model. Fault damage is above seismic resolution and can be modelled and interpreted on seismic.

In our DEM, at each time step, the total forces applied to a particle by its neighbours are used to compute its displacement. The particles are moved to their new positions by integrating their equations of motion using Newtonian physics and a Verlet numerical velocity scheme (Mora and Place, 1993). The particle assemblage is subjected only to elastic, gravitational and frictional forces, which results in the assemblage having no tensile strength and a purely frictional behaviour (Belheine et al., 2009; Botter et al., 2014). This is a reasonable behaviour for a km-scale, brittle upper crust full of discontinuities and at the verge of failure (Zoback, 2010). Compared to 2D, 3D modelling implies calculations in one extra dimension for each particle at each time step. This results in longer times of computation and restricts the minimum diameter of the particles to tens of meters for an assemblage at km-scale (Fig. 2). To bring the assemblage to reservoir depth, we apply an overburden traction at the top (Fig. 2). This traction should be updated every few time-steps such that it is always normal to the upper surface of the model (e.g., Botter et al., 2014). In 3D, this is difficult to implement and would drastically slow down the computation. To obtain results in a reasonable time, the overburden traction is applied vertically at the beginning of the simulation (Fig. 2a) and it is not updated afterwards. Fig. 2b shows the results after faulting. Although there is not a uniform distribution of the overburden tractions at the end of the simulation, faulting and associated folding in the assemblage are realistic.

As said before, one of the main challenges of the DEM is the calibration of the assemblage to make it behave as a real sedimentary rock at a few kilometres depth. While in 2D, biaxial and collapse simulations can be run to determine the bulk mechanical

properties of the assemblage (Botter et al., 2014), we do not have this capability in our DEM in 3D. Several studies describe numerical tests to define the bulk mechanical properties of DEM assemblages in 3D (Cheung and O'Sullivan, 2008; Belheine et al., 2009; Schöpfer et al., 2009, 2013; Cil and Alshibli, 2014), although these studies are at a smaller laboratory scale (cm to dm sample size). In order to obtain a reasonable mechanical behaviour of the assemblage at low cost and computational time, we studied the overall bulk behaviour of a homogeneous assemblage under boundary conditions similar to those of Fig. 2. We use two homogeneous assemblages that are intended to simulate competent (sandstone) and incompetent (shale) materials (Fig. 3). The dimensions of the assemblages are $1.45 \times 1.45 \times 0.45$ km. The assemblages consist of 150 000 particles of four radii from 7.5 to 12.5 m and with properties as specified in Table 1. The main parameter controlling the behaviour of the assemblages is the interparticle friction (Table 1). A vertical traction of 25 MPa is applied at the top of the model, corresponding to ~ 1.5 km sedimentary overburden, and a displacement boundary condition corresponding to a 65° dipping normal fault is imposed at the base of the model (Fig. 3). Fig. 3 shows cross sections of the simulations after 100 m fault displacement. The sandstone type assemblage shows a fault dip of 75° (Fig. 3 left column). The shale type assemblage presents a lower fault dip of $\sim 55^\circ$ and wider fault damage. These values are consistent with the properties (e.g. friction angle) of sandstone and shale (Zoback, 2010; Horsrud et al., 1998). We use these simulated sandstone and shale materials (Table 1) in Section 3.

2.1.2. Changes of properties

Faulting involves large and permanent strains. Few studies discuss the impact of large strains on seismic properties: in the laboratory at relatively low strains (Holt et al., 2008; Skurtveit et al., 2013), in samples of fault outcrops (Sigernes et al., 2002; Jeanne et al., 2012; Healy et al., 2014), and at a petroleum field scale (Hatchell and Bourne, 2005). Although these studies encompass a large range of lithologies, scales and deformation processes; they broadly illustrate how volumetric strain impact seismic velocities: compaction decreases porosity, thereby increasing density and seismic velocities, while dilation have the opposite effect. All the

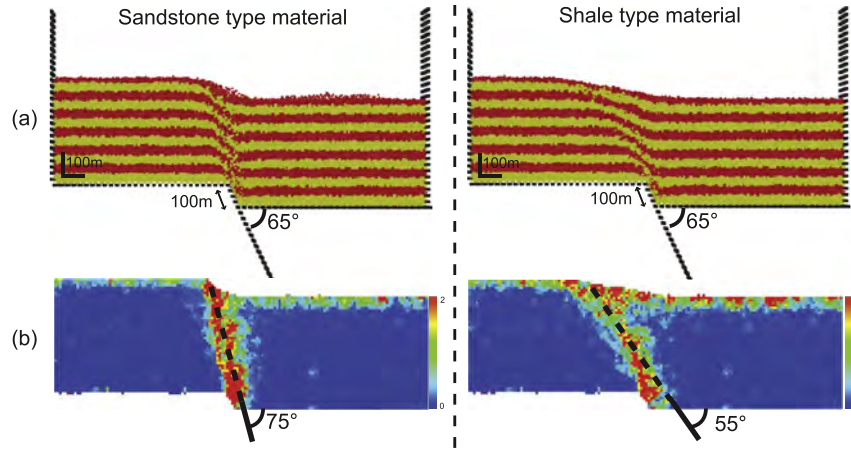


Fig. 3. Calibration of the sandstone type (left) and shale type (right) materials by measuring the fault dip in homogeneous assemblages of different interparticle friction (Table 1). (a) Geometry of a cross section after 100 m fault displacement. The layers are for visual purposes. (b) Shear strain and average dip of fault zone.

Table 1

Particles properties for the sandstone and shale type assemblages.

Input parameters:	Radii (m)	Density (kg/m ³)	Stiffness (GPa)	Friction
Sandstone	7.5–12.5	2500	166	0.40
Shale	7.5–12.5	2500	166	0.05

studies show a negative correlation between porosity and seismic velocity. However, there is no simple correlation between fault deformation, porosity, and seismic velocities. Data from Sigernes et al. (2002) on siliclastics and Jeanne et al. (2012) on carbonates show large variability in density and P-wave velocities in fault zones. Healy et al. (2014) show that in Oligocene-Miocene carbonates of the Mediterranean islands of Malta and Gozo, the facies of the host rock plays a major role in controlling these relationships, and the inner fault cores show lower porosity than the outer damage zones, supporting a negative correlation between fault deformation and seismic velocity. These measurements show a variation in wave velocity up to 50% in samples from fault zones. However, they may not only be due to faulting, but also to heterogeneities in the protolith and the fact that laboratory measurements from core samples can overestimate the values from the rocks in situ (Nes et al., 2000; Holt et al., 2008). Another problem is that our mechanical model provides bulk, meter size strain, which cannot be directly related to a smaller scale property such as porosity. In fact, the volumetric strains of our models (Section 3) are very large, and if they were directly converted to porosity, they would give nonsensical values. Volumetric strains in our DEM should be interpreted instead as the result of lower scale mesoscopic deformation: e.g. faulting, folding, joints, veins and cleavage development. Finally, there is the challenge of upscaling the rock properties to the typical low frequencies (20–40 Hz) and large wavelengths (10–100 m) of seismic data.

Given all these complexities, we estimate that a maximum change of properties due to faulting of $\pm 25\%$ is a reasonable value for our model scales and depths. We use in this study a simple, empirical relationship between volumetric strain, porosity and seismic velocity before and after faulting as described in Fig. 4 and similar to our previous work (Botter et al., 2014). This is a first order, probably inaccurate, approximation to the problem, but it allows us to compute in a reasonable manner the changes of rock properties due to large finite strain. Porosity, density, and seismic velocities are initially assigned to the sandstone and shale rock materials in the DEM before faulting (Table 2). These values are averages from

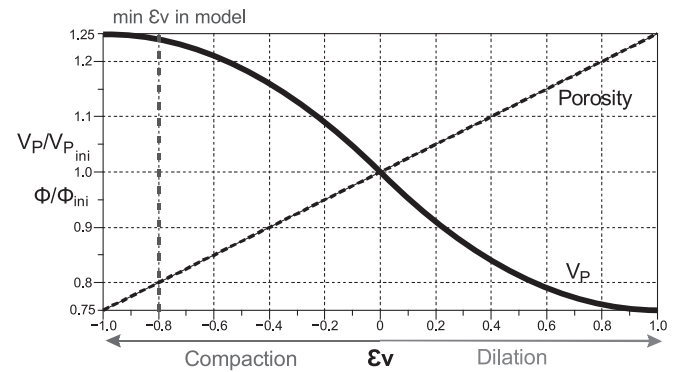


Fig. 4. Assumed change of porosity ϕ and P-wave velocity V_p with volumetric strain ϵ_v . ϕ_{ini} and V_{pini} are porosity and P-wave velocity before faulting.

the literature, for sandstone (Hoek and Brown, 1997; Mavko et al., 2009), and shale (Horsrud et al., 1998; Nygård et al., 2006), adapted to the scale and depth of the simulations. We use a nearest-neighbour routine (Cardozo and Allmendinger, 2009) to compute strain from the particle displacements in the DEM. After faulting, we relate the impact of volumetric strain on porosity with a linear relation (Fig. 4):

$$\phi = \phi_{ini}(0.25\epsilon_v + 1), \quad -1 \leq \epsilon_v \leq 1 \quad (1)$$

where ϕ is porosity, ϕ_{ini} is initial porosity and ϵ_v is volumetric strain. Although simplistic, a linear relation between volumetric strain and porosity can be considered as an acceptable approximation. Rock density ρ is then computed from porosity assuming water-saturated conditions:

$$\rho = \rho_g(1 - \phi) + \rho_w\phi \quad (2)$$

where ρ_g and ρ_w are grain and fluid densities respectively. P-wave velocity, V_p , follows a sigmoidal relation (Fig. 4):

Table 2

Acoustic properties assumed for the undeformed sandstone and shale materials.

	Φ_{ini}	ρ_g (kg/m ³)	$\rho_{tot\ ini}$ (kg/m ³)	V_{pini} (km/s)	V_{Sini} (km/s)
Sandstone	0.15	2650	2402.5	4	2.389
Shale	0.3	2700	2190	2	0.801

$$V_P = \begin{cases} V_{P_{ini}} \left(-0.25\varepsilon_v^2 - 0.5\varepsilon_v + 1 \right), & -1 \leq \varepsilon_v < 0 \text{ (compaction)} \\ V_{P_{ini}} \left(+0.25\varepsilon_v^2 - 0.5\varepsilon_v + 1 \right), & 0 \leq \varepsilon_v < 1 \text{ (dilation)} \end{cases} \quad (3)$$

where $V_{P_{ini}}$ is the initial P-wave velocity. A sigmoidal shape results in larger changes in velocities at smaller strains than at larger strains. This is consistent with laboratory measurements showing very large V_P changes at small strains (Holt et al., 2008; Skurtveit et al., 2013) and our hypothesis of maximum relative changes of $\pm 25\%$. Changes in V_S are directly related to changes in V_P through the Han's equation (Han, 1986) based on measurement from Sigernes et al. (2002) and Healy et al. (2014) showing a linear correlation between V_P and V_S .

2.1.3. Seismic modelling

Seismic imaging simulation is used to assess the impact of faulting on the resulting seismic image. The technique we use is a 3D pre-stack depth migration (PSDM) simulator (Lecomte, 2008; Lecomte and Kaschwich, 2008; Lecomte et al., 2015). This simulator acts as an image-processing method by distorting an input reflectivity grid to reproduce the effects of seismic imaging in PSDM mode (Fig. 5). The method properly handles diffracted energy and not only reflected one (Kaschwich et al., 2011), as opposed to 1D convolution. The PSDM simulator also works in the pre-stack domain and in depth, and correctly handles 3D effects in resolution and illumination as function of various parameters such as velocity model, survey geometry and wavelet. The method has been applied to faults and folds (Botter et al., 2014; Mascolo et al., 2015; Wood et al., 2015; Lecomte et al., 2015, 2016).

A complete description of this technique is given in Lecomte (2008). The structural input to the PSDM simulator is an incident-angle dependent reflectivity cube (Fig. 5a), which is obtained from the elastic properties of the model, i.e., density, P- and S-wave velocities. This volume is processed using ray-based modelling results (a calculation of the so-called illumination vectors; Gjøystdal et al., 2007; Lecomte, 2008) in the wavenumber domain in order to produce PSDM filters (Fig. 5b). These filters are dependent on factors such as survey geometry, wave frequency, direction and length of illumination vectors, and wave type. The PSDM filters are multiplied in the wavenumber domain to the reflectivity grid converted by FFT. A FFT^{-1} to this product gives the final simulated seismic image in the spatial domain (Fig. 5c). The conversion of the PSDM filters to the spatial domain gives point-spread functions

(PSFs), which are the image response of point scatterers (Fig. 5d). An equivalent process to the multiplication in the wavenumber domain is the convolution of the PSFs to the input reflectivity cube in the spatial domain in order to obtain the final seismic image (Fig. 5c–d). Compared to our previous study in 2D (Botter et al., 2014), the influence of the survey geometry (i.e. position of the streamers) is more significant in our 3D simulations. The overburden plays also a more important role in the final image, by influencing 3D wave propagation. All these effects are taken into account in the PSDM simulator. Being ray-based, robust and fast, the simulator allows efficient and near-interactive sensitivity analyses of these seismic parameters (Drotning et al., 2009).

2.2. Seismic interpretation

Once the seismic image of the fault model is obtained, the next step is to analyse and interpret the information. While in 2D we can use manual extraction techniques such as extracting seismic amplitude along a reflector and compare it to the corresponding elastic properties (Botter et al., 2014), this kind of analysis in 3D is implausible. Automated seismic attribute techniques can overcome this problem. The user can select adapted seismic attributes for best imaging the fault, and combine them in order to extract a fault geobody, allowing further analyses.

2.2.1. Seismic attributes

Seismic attribute mapping identifies variations in the amplitude and phase of the seismic wavelet and tracks these through the seismic cube. In general, seismic attributes applied to 3D post-stack seismic volumes improve the interpretation (e.g., Cohen et al., 2006; Chopra and Marfurt, 2007; Hale, 2013). For fault characterisation, several types of attributes can be considered. The first type deals with the orientation of seismic reflectors, and includes the dip, azimuth and tensor attributes (Hesthammer and Fossen, 1997; Jackson and Kane, 2012; Chopra and Marfurt, 2005, 2007 and references therein). Dip and azimuth are respectively the angle below the horizontal and the azimuth of a vector along the reflector's dip direction. These are calculated at each point (voxel) in the seismic volume, based on the maximum apparent dip (i.e. true dip) within a local volume around the point. The calculations use structural tensor techniques (e.g., Allmendinger et al., 2012). The azimuth units are degrees or radians, and the dip units are degrees or radians for seismic in depth. The tensor attribute is based on a structurally oriented tensor. The algorithm produces a symmetric tensor whose principal axes define the local reflector's orientation

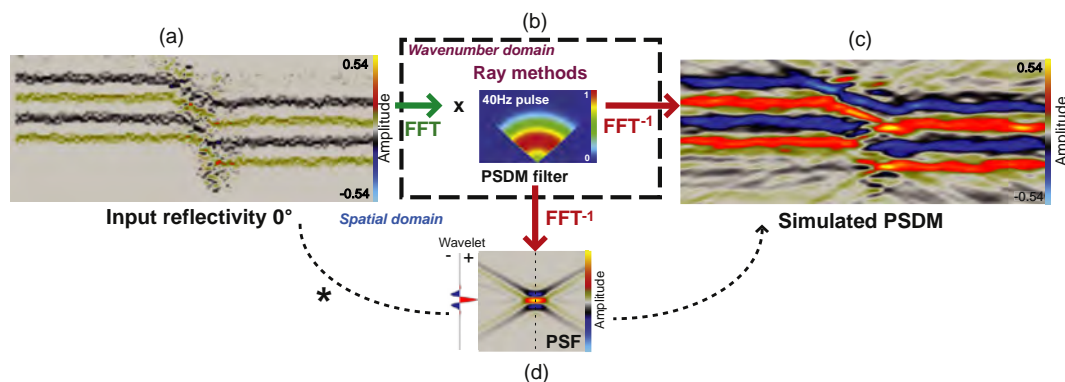


Fig. 5. Illustration of the PSDM simulator. (a) Input reflectivity grid in the spatial domain and conversion to the wavenumber domain using a Fast Fourier Transform (FFT). (b) Calculation of PSDM filter (colour scale corresponding to a normalized spectrum amplitude) in the wavenumber domain, using ray based methods. (c) Application of the PSDM filter to the input reflectivity in the wavenumber domain, plus inverse FFT (FFT^{-1}) on the result to produce the PSDM image. (d) Entire process is equivalent to convolution of the point spread function or PSF with the input reflectivity. The wavelet with its polarity is displayed for the centre of the PSF.

(Gersztenkorn and Marfurt, 1999). The attribute is a combination of the three eigenvalues of the tensor and identifies reflector discontinuity.

A second type of attribute deals with the continuity of seismic reflectors, mainly through the study of disturbance and incoherencies. The semblance attribute represents a measure of the coherence, i.e. similarity of traces within the seismic cube, to identify abrupt mismatches in amplitude along the reflectors (Bahorich and Farmer, 1995). Semblance is calculated along the seismic trace direction for a given number of traces. We use a structurally oriented semblance (SOS) algorithm as described in Iacopini and Butler (2011) and Iacopini et al. (2012, 2016). This algorithm is a further improvement of standard coherency and semblance multi-trace correlation calculations (Marfurt et al., 1998). SOS adapts to the local reflector's orientation to ensure that the semblance measure is taken perpendicular to the reflector, also extending the cross-correlation of traces beyond three adjacent traces (Sheriff, 1991; Marfurt and Chopra, 2007; Chopra and Marfurt, 2009). The algorithm accurately analyses structural and stratigraphic features over the entire volume, identifying subtle features that are not represented by peaks, troughs or zero crossings. The scale of the window of observation needs to be chosen by the user in order to capture details across the fault. These semblance techniques have been widely used for identifying subtle variations in seismic character, such as small faults (e.g., Marfurt et al., 1999; Chopra et al., 2000; Chopra and Marfurt, 2009). We use these two classes of attributes for fault interpretation. However, according to the situation, using only one attribute at a time can give an inaccurate mapping of the fault. To improve the fault interpretation, we combine the seismic attributes, getting a stronger definition of the fault zone (Purves and Basford, 2011).

2.2.2. Noise cancelation

Before starting the attribute analysis the seismic data need to be pre-conditioned in order to improve their quality or noise to signal ratio. In our workflow this stage is not essential as we work only with synthetic data, where the only noise is due to the migration generated by imperfect PSFs due to survey effects. Nevertheless, we carried out this step to remove the noise associated to the spherical particles boundaries in the DEM. To do so, we apply noise cancelation, especially removing coherent and random noise through two separated methods. The first method removes coherent noise in the image while at the same time preserving subtle details like edges, corners and sharp dip changes (Weickert, 1998; Marfurt et al., 1998). A structurally oriented noise filter is applied. This retains much more detail than non-structurally oriented smoothing techniques, as it uses dip and azimuth volumes to steer the smoothing. The second method uses an edge preserving diffusion filter in order to remove random noise and improve reflector continuity (Weickert, 1998; Höcker and Fehmers, 2002; Fehmers and Höcker, 2003). A tensor-based representation is used, implicitly allowing diffusion to be restricted within the local surface of the seismic reflector and not across it. The reflector dip is automatically calculated as part of the filtering operation; therefore pre-computed dip and azimuth attributes are not required for steering the filter. The diffusion tensor has a coherence-preserving behaviour, which tends to preserve and in some cases reinforce reflector offsets. The main reflectors are enhanced and smoothed as well.

2.2.3. Fault volume extraction

Once an improved “fault” cube has been obtained by noise cancellation and seismic attribute analyses, the next step is the extraction of the fault volume or fault geobody. To enhance the fault location and extent, a fault enhancement filter is applied to the

combined seismic attribute cube in order to improve the continuity along faults. The dimensions of the filter depend on the scale of the studied fault. The larger the dimensions, the broader the targeted fault zone. This filter is only a support for the next fault detection filter that turns the potential faults into fault planes. The fault detection filter applies a ridge detection algorithm laterally to identify potential faults and extract them as single voxel thick fault planes. The output volume shows the fault planes with a confidence factor printed on each voxel according to the input fault enhancement volume.

A geobody or 3D fault volume is then extracted, based on the fault skeleton and the combined seismic attribute cube. The geobody is based on a representation in which each voxel is “aware” of the data in its vicinity (Henderson, 2012). Starting with the seed voxels on the fault plane, the geobody is created by a growing process that adds new voxels to the volume. To be accepted into the geobody volume, a voxel needs to answer two criteria: 1. it must be a neighbour of any existing voxel of the geobody, and 2. the value of the attribute at that voxel needs to be greater than the local mean. An additional threshold limit can be added by the user to influence the growth of the geobody relative to the local statistics at each voxel.

Once the fault volume is collected, further steps can be applied for both qualitative and quantitative interpretation. For qualitative analyses, two techniques can be used (e.g. Iacopini and Butler, 2011): the first is to display the geobody back in the input data (seismic cube or elastic properties cubes) using only its contours or the full volume, in order to estimate the accuracy of the extraction process. A second way is to directly plot the input data in the 3D fault geobody. Quantitative interpretation can be done by converting the number of voxels in the geobody into metric units to give a gross rock volume value. It is then possible to compare the geobody volume to the fault volume extracted from the input properties cubes or run correlation studies.

3. Results

We apply the workflow to a DEM representing a $1.45 \times 1.45 \times 0.45$ km interbedded competent sandstone-incompetent shale sequence (shale layers are ~100 m thick; Fig. 2a). A north striking, 65° dipping normal fault is imposed at the base of the model, and an overburden traction of 25 MPa (~1.5 km depth) is applied at the top (Fig. 2a). The assemblage is composed of 150 000 particles with properties as described in Table 1. Starting with this initial model, two situations were studied: one in which the fault has constant displacement and another in which the fault displacement varies linearly from zero to a maximum along strike.

3.1. Constant fault displacement model

3.1.1. Mechanical modelling and property changes

Fig. 6 presents three east-west sections across the model after 100 m of fault displacement. These sections display the model geometry, shear strain, volumetric strain, and resultant changes of density and V_p or V_s (Fig. 6). The overall structure of the fault zone is similar along strike. Synthetic fault dips (Ferrill et al., 2005) develop adjacent to the fault. There is more faulting and thinning of the lower layers than of the upper ones (Fig. 6). The shear strain is higher and more localised at the base of the model, and the fault zone widens upwards displaying a monocline in the upper layers, similar to Withjack et al. (1990), Finch et al. (2004), and Ferrill et al. (2005, 2012). There are both dilation and compaction in the fault zone, with corresponding changes in density and seismic velocity (Fig. 6). Relative to the sandstone layers, the shale layers experience more compaction and density increase, but less increase in

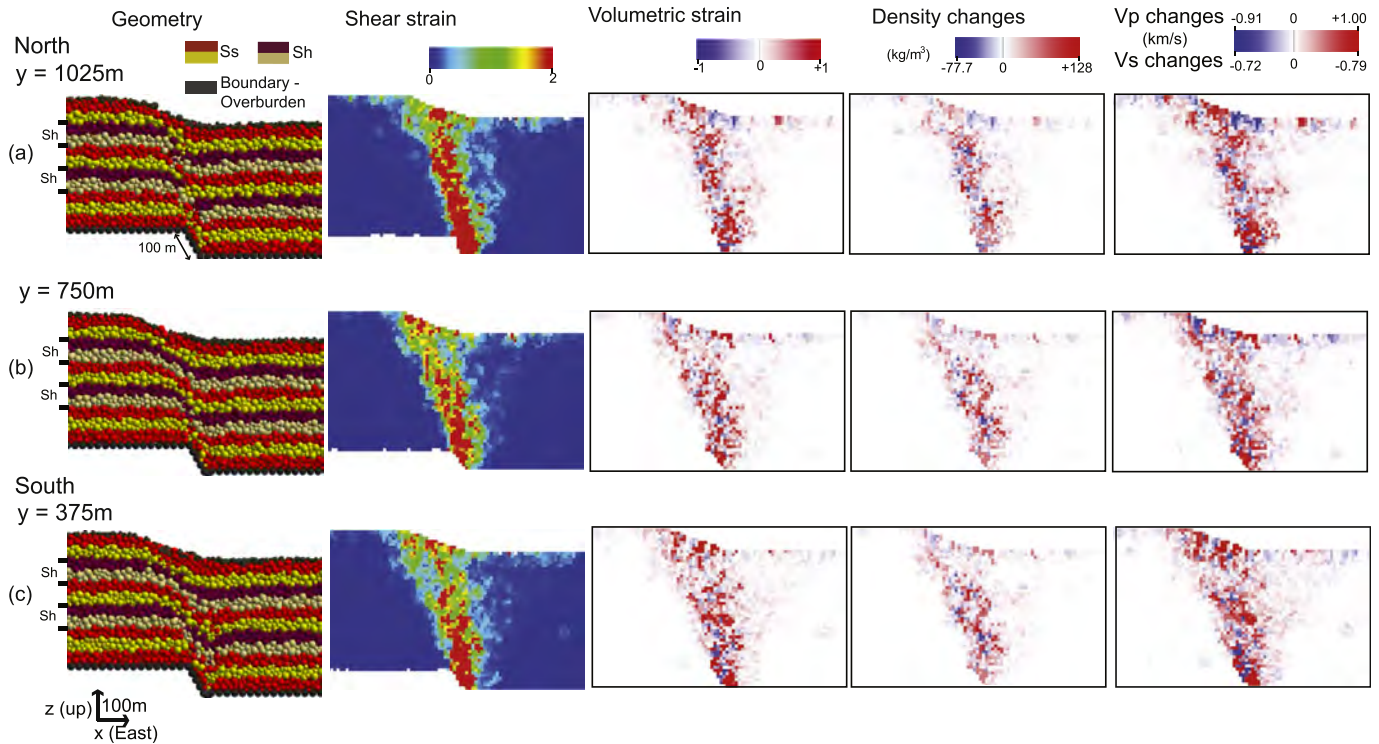


Fig. 6. East-west cross sections through the 100 m fault displacement model at (a) $y = 1025$, (b) $y = 750$ and (c) $y = 375$ m. First column is geometry, Ss = sandstone and Sh = shale layers, second column is shear strain, third column is volumetric strain, fourth and last columns are respectively the changes in density and in V_P and V_S due to volumetric strain.

seismic velocities. Even with similar fault geometry and fault displacement, there are some differences in geometry and strain between the cross sections. These variations are to some degree due to the differential stresses caused by the movement of the overburden particles at the top of the model.

3.1.2. Seismic modelling

The density, V_P and V_S of the model after faulting (Fig. 6) were used to compute a reflectivity grid with a 0° incident angle. This reflectivity grid is the input for the seismic imaging simulation. The PSDM simulator was applied for a 1.5 km thick, sandstone-like overburden with a V_P of 4.0 km/s and V_S of 2.4 km/s (Table 2), and zero-phase Ricker pulses of 10–40 Hz main frequency. The survey is at sea level and centred above the model, with five shot lines and nine streamers, a sufficient shot-receivers area to cover uniformly the entire model. For all the synthetic seismic cubes, the amplitude has been calibrated such that a reflectivity of intensity 1 corresponds to an amplitude value of 1 on the seismic image.

Fig. 7 presents the PSDM images for the three sections (cross lines) of Fig. 6 and four wave-frequencies (10, 20, 30 and 40 Hz), with their corresponding PSDM filters and PSFs. On all images, the layer interfaces are illuminated. At low wave frequency (10 Hz, Fig. 7), only the bottom reflectors corresponding to the bottom shale layer are offset. At $y = 1025$ m, however, the positive amplitude top reflector is offset. This is explained by higher fault deformation at this location (Fig. 6a). No further details can be extracted from these images to help identifying the fault volume. At 20 Hz more details are visible, and the reflectors are more distorted (Fig. 7). The geometry of the reflectors is more complex and the fault interpretation is not straightforward. At 30 Hz, the reflectors thin and are more irregular in the fault zone, especially towards the hanging wall (Fig. 7). In some reflectors, there is no clear offset. Diffractions are present mainly at the bottom of the model close to the fault, but also at the top, above the shale reflectors. Seismic

amplitudes vary in the cross sections, and higher amplitudes are visible at $y = 375$ and 750 m than at $y = 1025$ m (Fig. 7). At 40 Hz, the patterns and interactions of the reflectors are more detailed and complex. In all sections, almost all reflectors are offset and laterally distorted, which make harder to interpret the fault. Diffractions are visible at the top of the model, but also within the fault zone due to folding. The lateral extent of the fault zone can be estimated better in the high frequency images. However, defining exact boundaries is not possible using only the cross-lines. Low frequency data are more helpful to define the main fault slip plane than higher ones.

Fig. 8 presents three depth slices for wave frequencies from 10 to 40 Hz. At a low frequency of 10 Hz and on all three slices, the fault appears as a straight narrow zone separating the footwall and hanging wall. The dip of the fault can be estimated by looking at its x location, more on the west at the top of the model, and more towards the east at the centre and bottom of the model. At a higher frequency of 20 Hz, the fault is not anymore a narrow zone. There is a complex interaction between the footwall and hanging wall shale reflectors. At high wave frequencies of 30 and 40 Hz, the lateral interaction of the reflectors prevents any simple interpretation of the fault. The extent in x of this overlap is about 100 m at the bottom to 200 m closer to the top (30–40 Hz, Fig. 8), which corresponds to the lateral extent of the fault zone from the DEM model. Thus, the fault imprint on the seismic image can be further interpreted by the overlapping and distortion of the reflectors on depth slices, besides the offset between them on cross lines. This lateral extent can also be affected by the lateral resolution of the seismic, which can be estimated by the PSFs at the several frequencies (Fig. 8).

3.1.3. Seismic interpretation

The seismic interpretation workflow contains four steps: 1. Noise cancellation, 2. Seismic attribute analysis, 3. Geobody extraction, and 4. Correlation with input properties. Fig. 9a shows

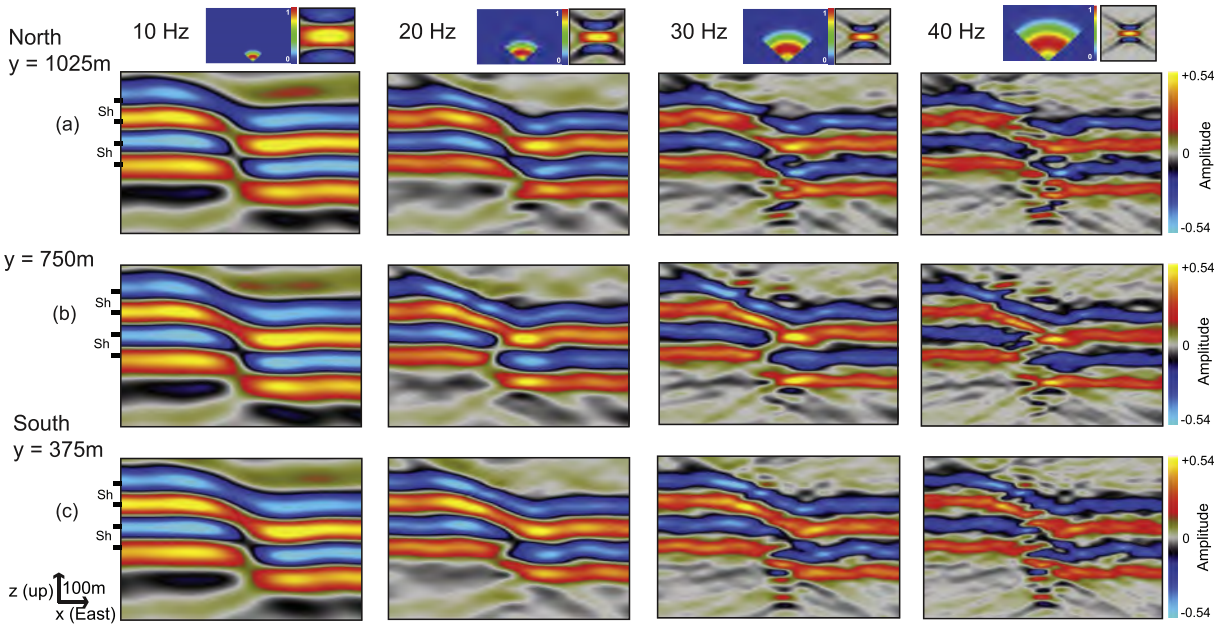


Fig. 7. PSDM seismic images of the 100 m constant fault displacement model for cross lines at (a) $y = 1025$, (b) $y = 750$ and (c) $y = 375$ m. Columns correspond to four wave frequencies, 10–40 Hz. At the top of each column, the PSDM filter and corresponding PSF are shown.

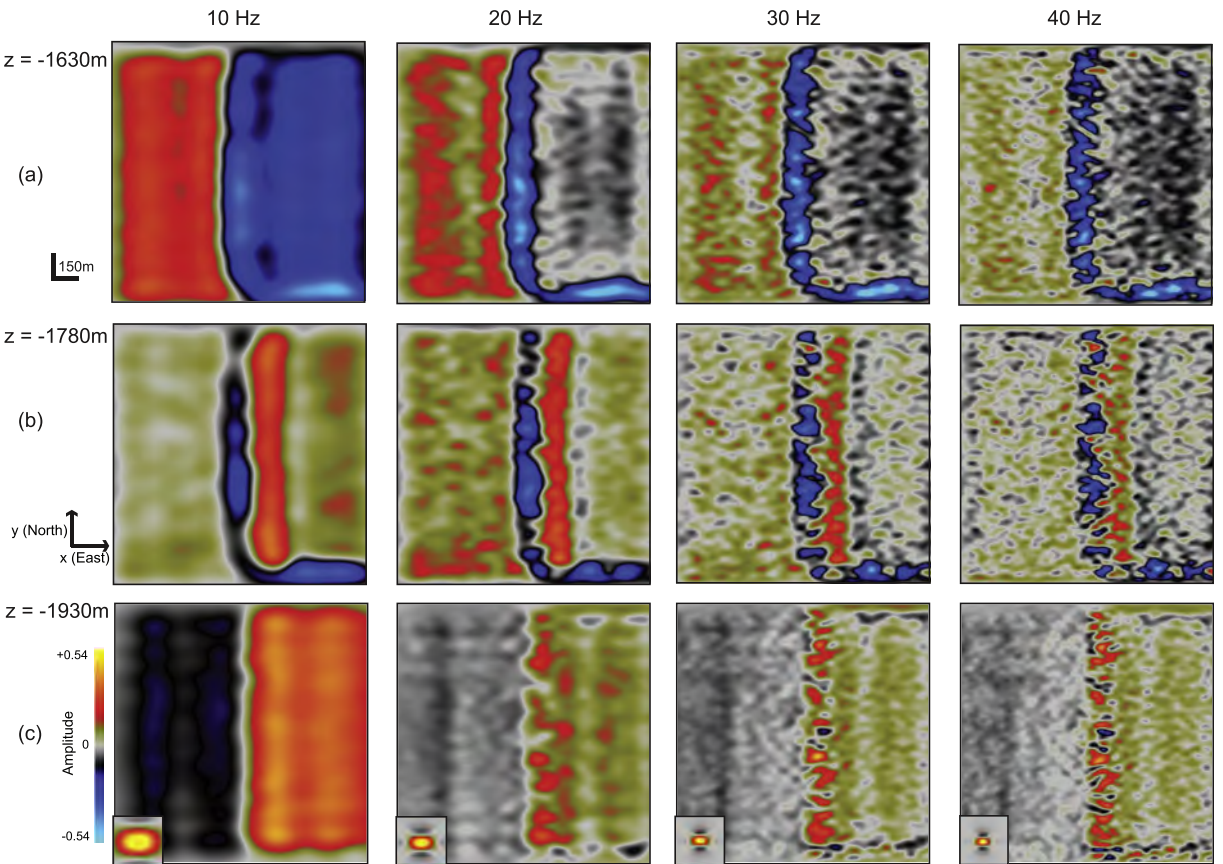


Fig. 8. PSDM seismic images of the 100 m constant fault displacement model for depth slices at (a) $z = -1630$, (b) $z = -1780$ and (c) $z = -1930$ m. Columns correspond to four wave frequencies, 10–40 Hz. The corresponding PSFs in depth view are shown on the bottom left corner of the bottom seismic images.

the application of noise cancellation to the 40 Hz seismic cube. Whilst our ideal synthetic cube does not present noise, this step removes the fluctuations along the reflectors (e.g. noise due to the

spherical particles of the DEM), allowing focusing only on the fault zone. It also removes the main random and coherent noise within the fault zone without affecting its main imprint.

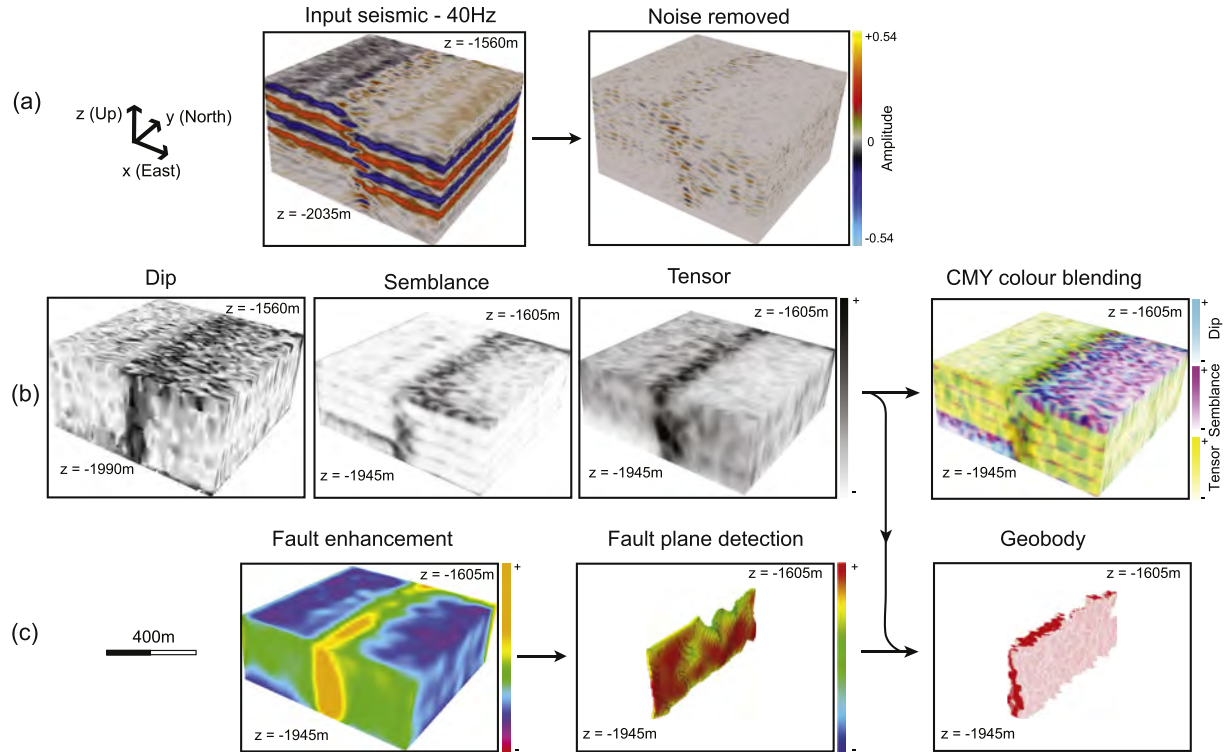


Fig. 9. Seismic attributes based workflow: (a) Noise cancellation of the 40 Hz seismic cube. (b) Dip, semblance and tensor seismic attributes applied to the noise cancelled cube and combined in a cyan-magenta-yellow (CMY) colour blending cube. (c) Geobody extraction by applying a fault enhancement to the CMY colour blending cube, defining a fault plane and combining it with the fault enhancement volume to extract the geobody.

We ran three attributes on the noise-cancelled cube: dip, semblance and tensor (Fig. 9b). These attributes help to enhance the fault zone for further extraction. The dip attribute highlights the changes of reflector dip within the fault zone. The higher values of the dip (dark colour in Fig. 9b) show a sub-vertical structure. Some features away from the fault in the hanging wall are also highlighted. The semblance attribute identifies discontinuities in the reflectors, mainly defining the fault zone and layer interfaces, although boundary effects are also highlighted (Fig. 9b). The tensor attribute provides the ability to define the fault area, and since it follows the local structural gradient, it positively defines the fault zone (Fig. 9b). To improve the definition of the fault zone, we combine these three attributes. The cyan-magenta-yellow (CMY) cube in Fig. 9b is the colour-blending cube of the attributes: dip in cyan, semblance in magenta and tensor in yellow. The darker the colour is, the higher is the probability of the fault zone.

The next step is to extract a fault geobody based on this CMY cube (Fig. 9c). The fault enhancement cube defines the probability to find a fault within the higher CMY values, which creates a large and smoothly defined zone. From this cube a one voxel thick fault plane containing the highest probabilities is extracted (Fig. 9c). The fault plane and the CMY cube are combined in a “growing” algorithm that detects the high probability voxels around the fault plane to extract the geobody. This geobody represents the most probable fault volume based only on the seismic image and the parameters of the attributes analysis.

Once the fault geobody is extracted, we can qualitatively assess its accuracy by displaying it back in the seismic and velocity cubes (Fig. 10a and b). Three techniques are used here: first, we display the boundaries of the geobody within the property cube; second, we plot the entire geobody volume back in the cube; and finally we display the input properties within the geobody (Fig. 10). Plotting the geobody back in the seismic data (Fig. 10a) is a necessary control

of the interpretation workflow. The contours of the geobody show that the workflow captures the central part of the fault corresponding to the higher distortion of the reflectors. In map view, the geobody follows the interaction pattern between the footwall and hanging wall reflectors. However, the lateral extent of the geobody (about 100 m) corresponds mostly to the highest deformation area of the fault and not to the entire zone (Fig. 10a). The geobody might then correspond to the diffraction from the seismic cube, but still manages to capture the complexity of the fault zone from the seismic. Having the geobody back in the input velocity cube (Fig. 10b) is a first qualitative correlation between the seismic data and the P-wave velocity. The geobody corresponds to the highest change of velocity of the model, but it does not capture the entire lateral extent of it (Fig. 10b). In our case, largest changes in V_p indicate faulting, so the geobody is a direct representation of the fault. When looking at V_p displayed back in the geobody (Fig. 10b, right), we notice that the shape of the geobody is directly linked to the rock properties within the sequence. The geobody bends towards the footwall (west) where in contact with the shale layer on the hanging wall, and towards the hanging wall (east) where in contact with the shale layer on the footwall. This could help determining the lithology of the section in a layered sequence of competent and incompetent rock materials.

As a first step towards a more quantitative interpretation, we plot in Fig. 11 the seismic amplitude versus the volumetric and shear strain of the DEM for both the entire seismic volume (grey dots) and the extracted fault geobody (dots colour coded by fault enhancement) at 40 Hz. For seismic amplitude versus volumetric strain (Fig. 11a), the seismic volume varies through the entire range of amplitude values, but is mainly restricted to a volumetric strain between -0.2 and 0.2 (Fig. 11a). The geobody contains a kernel of values at low amplitude (-0.15 to 0.15) and volumetric strain (-0.2 to 0.2). This group presents mainly low values of fault

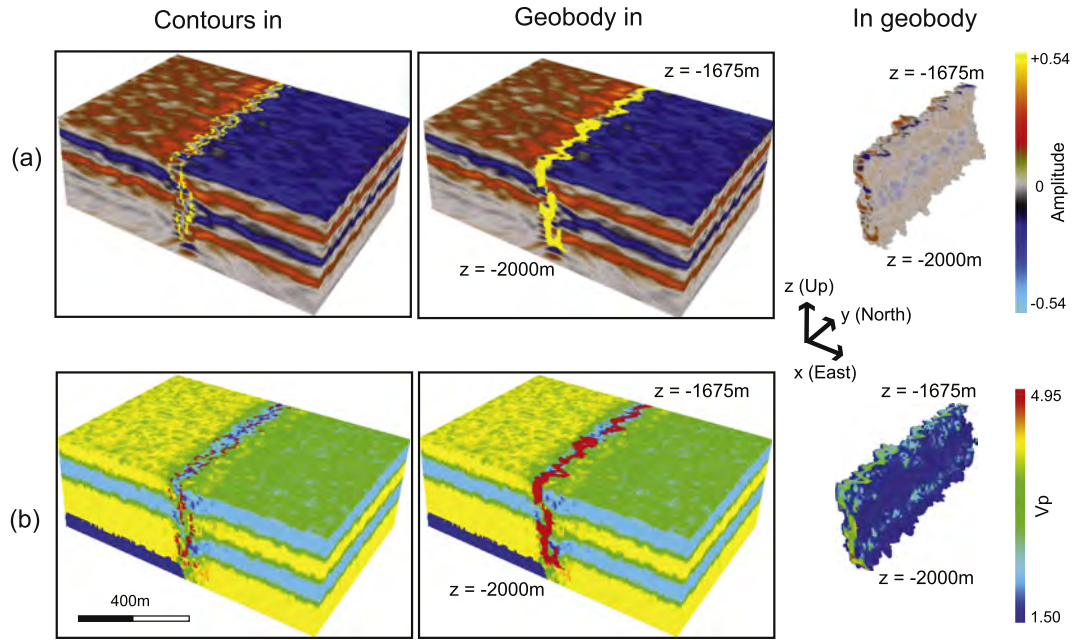


Fig. 10. Geobody in (a) the input seismic cube and (b) the input velocity cube. Left column displays the contours of the geobody, middle column displays the whole geobody, and right column display the property cube in the geobody volume.

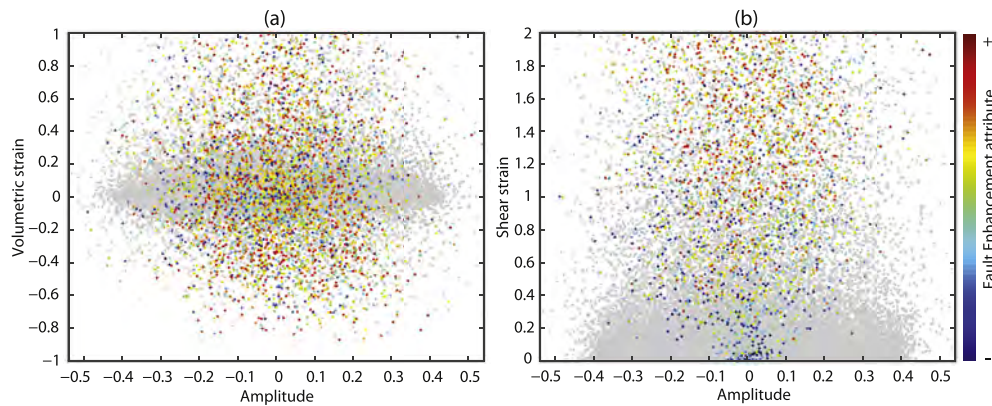


Fig. 11. Seismic amplitude versus volumetric strain (a) and shear strain (b) for the constant fault displacement model. The grey dots correspond to the entire seismic volume. The dots corresponding to the geobody are colour coded by the fault enhancement attribute (red = high, blue = low). (For interpretation of the references to colour in this figure legend, the reader is referred to the web version of this article.)

enhancement. The other geobody values are spread around this kernel with larger volumetric strains. Overall, high fault enhancement values correlate with high volumetric strain. Fig. 11b shows seismic amplitude versus shear strain. Most of the seismic volume is below a shear strain of 0.4. The geobody spreads out from low values of amplitude and shear strain to higher values. Below shear strain values of 0.4 the geobody has mostly low fault enhancement values. While there is a large variability within the geobody, the larger values of shear strain correspond almost systematically to high fault enhancement values.

3.2. Linearly variable fault slip model

3.2.1. Mechanical modelling and property changes

Starting with the same initial assemblage (Fig. 2a), we run a simulation with linearly variable fault slip along strike (Fig. 1a). At the end of the simulation, the southern part of the model has no fault displacement whereas the northern part has 140 m. Fig. 12 shows the geometry, shear and volumetric strain, and property

changes on three east-west cross sections across the model. The southern cross section (Fig. 12c) has only 36 m of fault displacement. Here the fault zone in the lower part of the sequence dips west, opposite to the imposed fault boundary. Volumetric strain shows mainly high dilation and almost no compaction. With higher displacement (72 m) at the middle of the model (Fig. 12b), the fault has accumulated enough strain to form a zone 100 m wide with average dip angle of 75° east. Volumetric strain shows dilation, especially in the sandstone layers, and more compaction in the bottom shale layer. At large fault displacement (100 m) on the northern section (Fig. 12a), the fault has a similar structure than the constant fault displacement model (Fig. 6), with faulting in lower layers and folding in upper layers. The shear and volumetric strain have high values in the lower and middle part of the model, but not in the upper part. Property changes have the same behaviour than in the constant model: higher compaction in the shale layers and relatively less changes in seismic velocities compared to the sandstone layers (Fig. 12).

Fig. 13 shows the geometry and shear strain of three depth slices

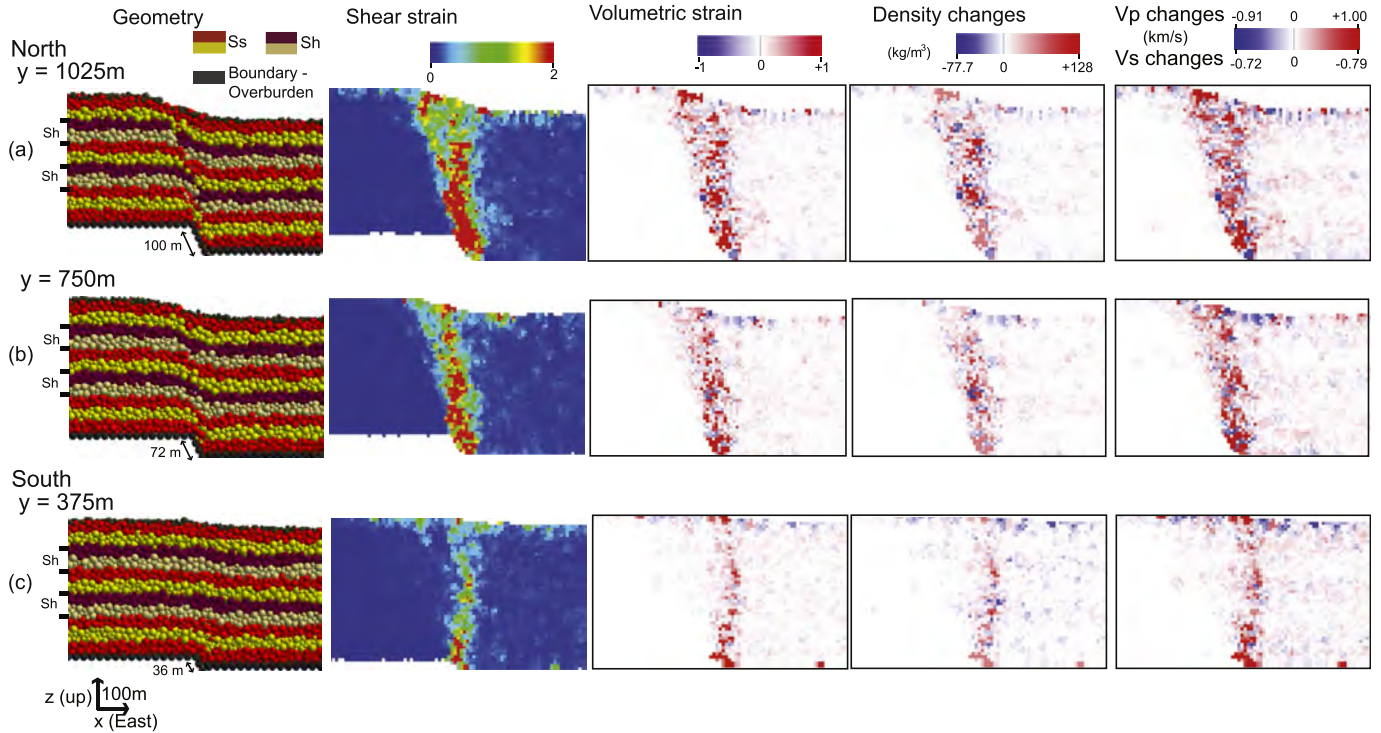


Fig. 12. East-west cross sections through the linearly variable fault displacement model at (a) $y = 1025$, (b) $y = 750$ and (c) $y = 375$ m. First column is geometry, Ss = sandstone and Sh = shale layers, second column is shear strain, third column is volumetric strain, fourth column is density changes and fifth column is V_p and V_s changes due to volumetric strain.

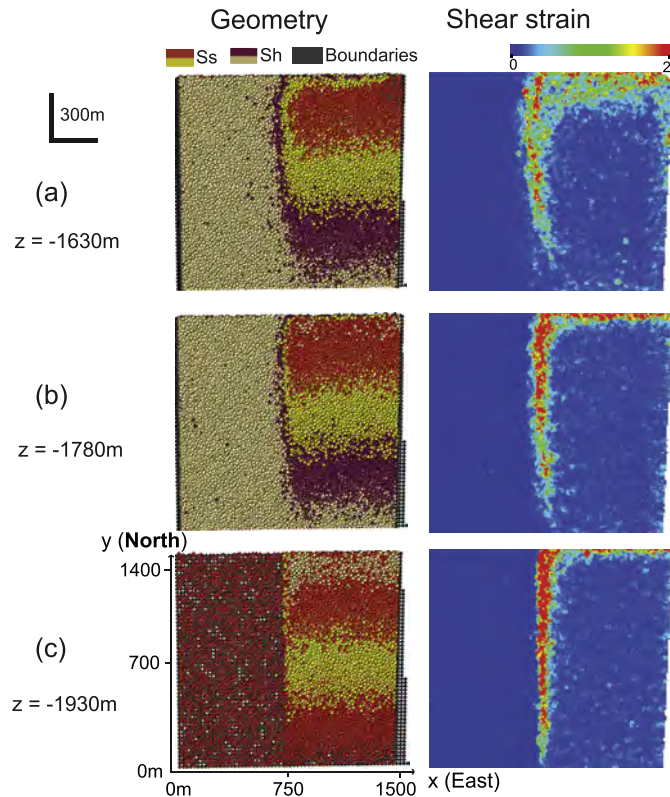


Fig. 13. DEM depth slices through the linearly variable fault displacement model at (a) $z = -1630$, (b) $z = -1780$ and (c) $z = -1930$ m. Left is geometry, Ss = sandstone and Sh = shale, and right is shear strain.

across the model. The deepest slice (Fig. 13c) is located close to the bottom boundary particles, and presents a straight and narrow (<100 m) fault zone that decreases in extent from north to south. In the middle depth slice (Fig. 13b), the fault zone is wider (~150 m in the north) and in southern areas slightly curves towards the east due to the reverse nature of the fault zone at low fault displacement (Fig. 12c). In the shallowest depth slice (Fig. 13a), folding is more important and the fault zone is much wider (about 250 m in the north). On all three slices, high values of shear strain (~2) gives a good indication of the fault tipline location at about $y = 450$ m in the upper slice and $y = 200$ m in the lower slice (Fig. 12).

3.2.2. Seismic modelling

The density, V_p and V_s after faulting were used to compute a reflectivity grid with a 0° incident angle. We used the same overburden, zero-phase Ricker pulses and survey geometry than in the constant fault slip model. Fig. 14 presents the three cross-lines corresponding to the three sections of Fig. 12, at four wave frequencies from 10 to 40 Hz. At small displacements (Fig. 14c), the fault does not show in the low frequency images (10 and 20 Hz), as the displacement is lower than the vertical resolution (50–100 m). At 30 Hz, we can observe some thinning of the reflectors in the fault zone. At the top of the model, some fault related diffractions are visible. At 40 Hz, more diffractions are present and the geometry of the lower reflectors is defined better. At 36 m fault displacement, it is difficult to interpret a fault from the cross-lines, as the fault is almost at the limit of seismic vertical resolution. At higher fault displacement (72 m, Fig. 14b), all reflectors are folded enough to suggest a fault zone, at any frequency. At a high wave frequency of 40 Hz, the reflectors closely follow the sandstone-shale interfaces from the DEM. Fault related diffractions are also much more visible. At large fault displacement (100 m, Fig. 14a), the seismic images look similar to those of the constant fault model (Fig. 7). At low

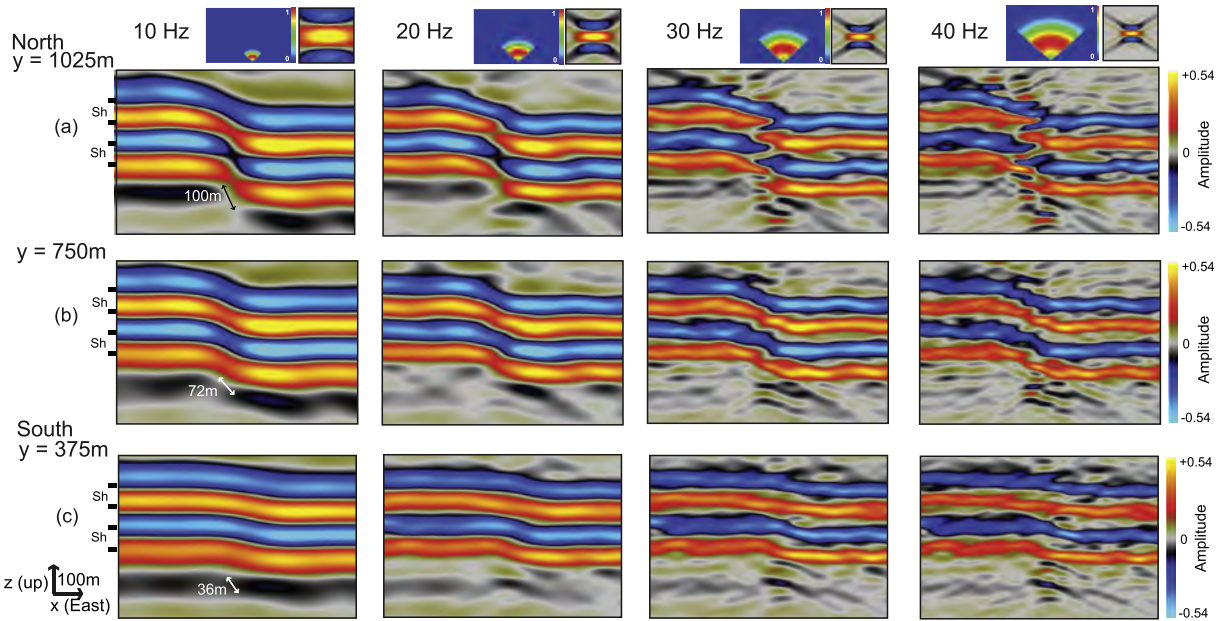


Fig. 14. PSDM seismic images of the linearly variable fault displacement model for three cross lines at (a) $y = 1025$, (b) $y = 750$ and (c) $y = 375$ m. Columns correspond to four wave frequencies, 10–40 Hz. At the top of each column, the PSDM filter and corresponding PSF are shown.

frequencies of 10–20 Hz, the positive amplitude reflectors are slightly offset. At high frequencies of 30–40 Hz, there is interaction between the reflectors from the hanging wall and footwall, and diffractions associated to the fault are visible.

Depth slices are important to define the width of the fault zone and the fault tipline. The three depth slices of Fig. 13 are displayed in Fig. 15 for wave frequencies from 10 to 40 Hz. At the bottom of the model (Fig. 15c), and only at wave frequencies of 20 Hz and

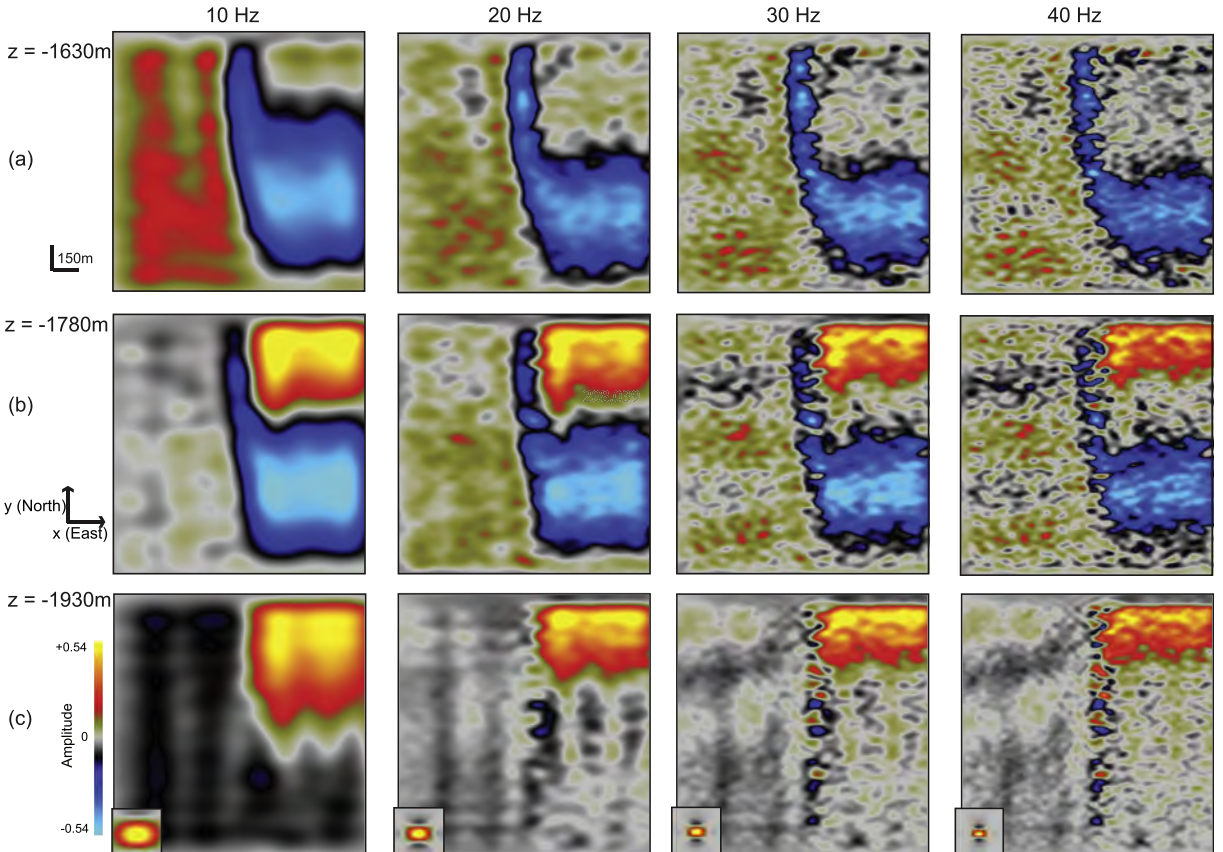


Fig. 15. PSDM seismic images of the linearly variable fault displacement model for three depth slices at (a) $z = -1630$, (b) $z = -1780$ and (c) $z = -1930$ m. Columns correspond to four wave frequencies, 10–40 Hz. The corresponding PSFs in depth view are shown on the bottom left corner of the bottom seismic images.

above, it is possible to identify reflections from the fault zone. These reflections indicate a straight and narrow fault zone, from 100 to 250 m wide, much as it is depicted by the shear strain at this depth (Fig. 13c). At 30–40 Hz, it is even possible to follow south the fault reflections to approximately locate the fault tipline. In the middle slice (Fig. 15b), we can observe in southern regions the bending of the fault towards the east (similar to Fig. 13b), but it is harder to define the fault tipline. The lateral extent of the fault zone can be estimated by looking at the overlap of opposite phase reflectors from the hanging wall. This is clearer at high frequencies (30–40 Hz). In the shallowest slice (Fig. 15a), the bending of the fault towards the east in southern regions is clear, as well as the lateral extent of the fault zone. By studying cross-lines and depth slices, we can extract some information about the fault structure, although it is not possible to precisely define the boundaries of the fault zone.

3.2.3. Seismic interpretation

The same noise cancellation step applied to the constant fault slip model (Fig. 9a) was applied to the 40 Hz seismic cube of the variable fault slip model. Seismic attribute analyses were then run on this noise free cube. Dip, semblance and tensor attributes with

the same conditions than those for the constant fault slip model, were applied to the variable fault slip model (Fig. 16a). The dip attribute captures a lot of dip variations in the upper part of the hanging wall, most probably induced by the overburden effect. The semblance attribute highlights the fault zone as well as the layer interfaces and the overburden and bottom areas. Only the tensor attributes captures just the principal structural changes associated to the fault (Fig. 16a). Darker colours in The CMY colour blending cube are centred on the fault zone as well as on the overburden (Fig. 16a).

The geobody was then extracted using the same methods as in the constant fault slip model. The geobody is displayed back in the seismic data (Fig. 16b) and in the P-wave velocity cube (Fig. 16c). The geobody's contours in the seismic show that the overburden and bottom boundaries are part of the geobody. These parts are taken away in order to focus only on the fault zone (In geobody, Fig. 16b–c). The extracted geobody has larger lateral extent at larger fault displacements towards the north. The contours of the geobody follow the reflectors offsets and capture the reflectors distortion/interaction in the fault zone, highlighting its complexity (Fig. 16b). The delineation of the fault tipline, towards the southern end of the geobody corresponds to $y = 240$ m and 23 m fault displacement in

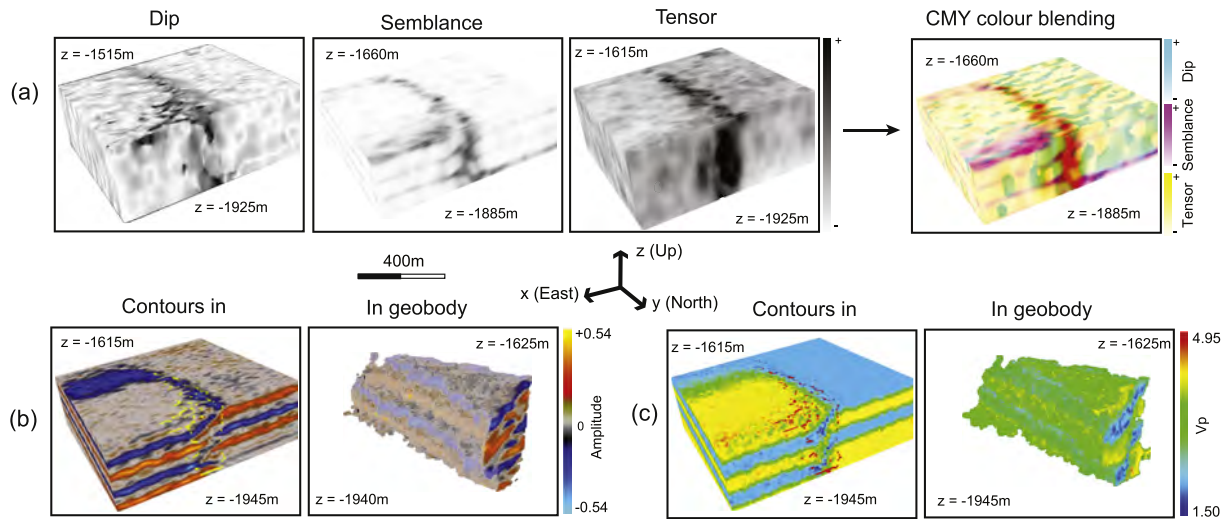


Fig. 16. Seismic attributes analysis based on a 40 Hz seismic noise cancelled cube of the linearly variable fault displacement model: (a) Dip, semblance and tensor attributes combined in a CMY colour blending cube. (b) Extracted geobody back in seismic cube, using contours and displaying seismic data within geobody. (c) Extracted geobody back in velocity cube, using contours and displaying property within geobody.

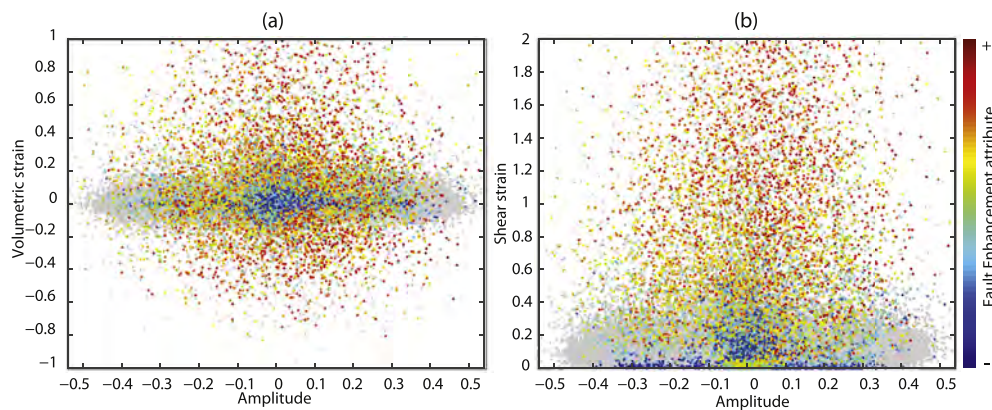


Fig. 17. Seismic amplitude versus volumetric strain (a) and shear strain (b) for the linearly variable fault displacement model. The grey dots correspond to the entire seismic volume. The dots corresponding to the geobody are colour coded by the fault enhancement attribute (red = high, blue = low). (For interpretation of the references to colour in this figure legend, the reader is referred to the web version of this article.)

the lower part of the geobody, and $y = 470$ m and 45 m fault displacement in the upper part, which is fitting the observations from the DEM depth slices (Fig. 13). This means that at 40 Hz, the interpretation workflow takes into account reflectors dipping and thinned towards the fault zone (Fig. 14c). The geobody's contours back into the P-wave velocity cube show that the geobody captures most changes in velocity (Fig. 16c). As in the constant fault slip model, there are protuberances of the geobody away from the shale layers in both the footwall and hanging wall, which can help interpreting lithology from seismic.

Fig. 17 shows seismic amplitude versus volumetric and shear strain. The distribution of the entire seismic volume is similar to the one from the constant fault displacement model. For seismic amplitude versus volumetric strain (Fig. 17a), most of the strain values are between -0.2 and 0.2 . The geobody presents an ellipsoid-shaped kernel of low fault enhancement values for low values of amplitude and volumetric strain. Fault enhancement values increase concentrically around this low probability kernel, where high fault enhancement values correspond to large volumetric strains. In the seismic amplitude versus shear strain graph (Fig. 17b), some of the geobody values plot along shear strain -0 for the full range of amplitude values. Here the fault enhancement values are low, although there are some high values around 0 amplitude (Fig. 17b). From this low shear strain, the geobody spreads upwards for larger values of shear strain (Fig. 17b). Large values of shear strain, i.e., >0.4 , present exclusively high fault enhancement. This large fault enhancement values are mostly concentrated around low seismic amplitudes (-0.2 to 0.2 , Fig. 17b), which is explained by the fact that the fault zone is characterised by offset of the reflectors and low amplitudes. In comparison to the constant fault slip model (Fig. 11b), fewer high shear strain values in the seismic volume are not included in the geobody (Fig. 17b), which suggests a stronger correlation between the fault enhancement attribute and shear strain.

4. Discussion and conclusions

We have presented a synthetic methodology to study the impact of 3D fault zone architecture and properties on seismic images and their interpretation (Fig. 1). Fault models were simulated with a DEM (Fig. 1a), which allowed us to study faulting and associated deformation at large scale and the impact on fault deformation of parameters such as rock competence, overburden stress and fault displacement gradients along strike. The method does not intend to reproduce specific outcrops, but rather produce analogue fault geometries and strain fields that could be encountered in subsurface siliclastic reservoirs. A simple calibration phase was run in order to define assemblages with bulk frictional properties similar to those of sandstone and shale. The main controlling particle parameter on the bulk competence of these rock materials is the interparticle friction (Table 1). Simple, empirical relationships were used to modify the initial properties of the rock materials due to volumetric strain (Figs. 1b and 5). These are clearly a first order approximation, but given the complexity of the problem and the issues with upscaling, they are a reasonable way to transfer the information from the DEM to a reflectivity cube. Computing limitations make the particles in our DEM models quite large (Table 1). This has impact on the resolution of the model and the simulated fault architecture. Botter et al. (2014) show that smaller particles result in better definition of fault segments and fault architecture. This can be very important for defining high strain areas, for example the fault tipline in the variable fault displacement model (Fig. 13).

All the seismic imaging and interpretation are dependent on the quality of our fault models. By using the DEM modelling and the

simple empirical laws to change the elastic properties (Fig. 5), we are limited in the outcome of our fault models, and we obtain models that are a representation of faulting influenced by fault-propagation folding. Maximum fault throws can be observed at the base of the model, and widening of the fault zone and folding in the upper layers (Figs. 6 and 12). The shear strain shows that, as the amount of fault displacement increases, the fault propagates upward and displaces the upper layers (Figs. 6a and 12a). However, this displacement is not uniform in the constant displacement model along strike, which can be explained by the mechanical contrasts in the layers and by the non-uniform distribution of the overburden particles at the end of the simulation (Fig. 6). These results, even though at different scale and in 3D, are in line with the analogue experiments of Withjack et al. (1990), where force folding in wet clay models widens upwards and secondary faults form, even if the main faults have not breached into the shallower part of the model. The resolution of our DEM models does not allow us, however, to identify secondary faults and fractures. DEM simulations by Finch et al. (2004) in extensional settings show hanging wall synclines and footwall anticlines adjacent to the fault that can also be observed in our models. Moreover, they show that the fault zone width is controlled by the strength of the material and the fault dip angle, and that for layered sequences, there is earlier faulting in the more competent layers than in the weaker ones. Our fault models also show similarities to seismic scale outcrops. The Big Brushy Canyon monocline, Sierra Del Carmen, Texas (Ferrill et al., 2005), is an example of a fault-propagation fold with a normal fault of maximum displacement 100–500 m over 10 km, with a base clay-rich layer displaced and thinned, and two overlying limestone units that are folded and not uniformly faulted. The high dip angle fault ($>75^\circ$) does not breach the upper limestone unit (Ferrill et al., 2005, 2007). 2D finite element models of this outcrop (Smart et al., 2009) provide much more details about the strain distribution than our fault models (Figs. 6 and 12), but our models are in 3D and present also a variation of fault displacement along the strike. Another example is the seismic-scale Hadahid fault system in Western Sinai, Egypt (Lewis et al., 2015). Here, a 30 km long, NW-SE trending, W dipping basin-bounding normal fault system exhibits a large-scale monocline, which in some areas is breached by the fault system and in others is not. Trishear modelling of the monocline shows that fault displacement varies from 800 to 200 m along strike (Cardozo et al., 2011). We can also point similarities of our models to the Smørbukkk field area, Halten Terrace, Mid-Norway, where a monocline above a basement-involved normal fault dying out along strike is clearly imaged in 3D seismic (Corfield and Sharp, 2000).

The PSDM simulator was applied to the two derived reflectivity grids (Fig. 1c). Only the impact of wave frequency on the resultant seismic image is presented here. All other parameters, such as the survey type, wave type, background media, illumination direction, and overburden, which can have a large impact on the images, were kept constant. These parameters are worth exploring within the same framework. The wave frequencies used are representative of reservoir depths, but frequencies higher than 30 Hz can sometimes be harder to obtain in reservoir exploration. In general, the lower the wave frequency, the higher the tendency to image the fault as a surface. Fault related diffractions are present at high frequencies of 30–40 Hz. These, together with the distortion and interaction of reflectors in the fault zone, allow approximately defining the fault architecture, especially by combining cross lines and depth slices.

Seismic interpretation (Fig. 1d) relies on tools usually applied to post-stack seismic data (Chopra and Marfurt, 2005), which can contain more noise. Our simple models may not be applicable to these cases. The seismic data usually available to the interpreter is the stacked-data volume. In this situation, it is considered that each

stacked trace exhibits the same reflection character as that of a single source–receiver pair with no offset. In our 0° incident angle PSDM seismic cubes, the offset is null. We can therefore apply all structural and orientation seismic attributes (dip, tensor and semblance) to the fault characterisation. This makes our workflow adaptable to real seismic data. Chopra and Marfurt (2005) show that multiple attributes analyses need to be used carefully, such as the choice of attributes is independent of one another. The dip and tensor attributes are not independent, as the dip is based on tensor gradient computations, however the information displayed by the dip and the tensor attributes is different (dip shows reflector angle, tensor shows variability in reflector orientation), resulting in the tensor attribute helping to refine the definition of the fault zone (Figs. 9 and 16). By limiting our choice to three attributes, we target the necessary aspects of seismic for fault characterisation, such as dip, structural changes and variations of the reflectors amplitude. This choice is also based on the combination of seismic attributes usually applied to real seismic data for fault identification (e.g., Chopra and Marfurt, 2005; Dutzer et al., 2010; Iacopini and Butler, 2011; Iacopini et al., 2012, 2016). The seismic interpretation workflow is very much dependent on the quality of the PSDM cubes. By using the same attribute combination on the two models, we obtain different fault geobodies, one capturing only the inner fault zone (constant fault slip model, Fig. 10), and another capturing features outside the fault zone (variable fault slip model, Fig. 16). This is mainly due to the higher strains present in the variable fault slip model away from the fault zone. Thus during interpretation, one needs to fine-tune the attribute configuration in order to capture either the inner fault related features or the more extensive fault associated deformation. However, seismic attributes can enhance subtle noise, therefore, to expand the application of this visualisation workflow to real datasets, one needs to be familiar with the acquisition and processing steps applied to the seismic data and with the assumptions behind the attributes in order to avoid pitfalls in the structural interpretation (Marfurt and Alves, 2015).

Relating seismic amplitude in the geobody to the DEM derived strains is an important step for understanding the fault internal properties (Fig. 1e). Although the geobody captures a large range of volumetric and shear strains (Figs. 11 and 17), the higher probabilities to get a fault (high fault enhancement values) correspond mostly to the larger strains. This does not help, however, to retrieve directly the strain from the amplitude values, as an amplitude value can be associated to different levels of strain. Figs. 11 and 17 are just proxies for the distribution of rock properties in the fault zone. With only these data available, an interpreter cannot invert directly the seismic data for petrophysical properties or facies studies. Studies investigating the trapping potential of fault-related-folds do not use only seismic data. Kostenko et al. (2008) show an exceptional example combining seismic, well log and dipmeter data, and geological restoration to determine the actual trap geometry and fault sealing capabilities of a thrust related anticline in the Niger Delta. Dutzer et al. (2010) propose a visualisation of fault sealing mapped on 3D fault volumes of an underground gas storage field. They use seismic attributes constrained to abundant well log data. Thus, in order to find a relation between the fault damage mapped in seismic and the actual rock properties, one would need more information from well data, localised seismic surveys, and probably seismic inversions.

Compared to our previous work in 2D (Botter et al., 2014), the 3D workflow presented here is more advanced, exploring different aspects of 3D mechanical and seismic modelling, and seismic interpretation. Sensitivity analysis of the impact of seismic wave frequency gives unique information on how the fault architecture can be perceived at different seismic resolutions. At low frequencies, the fault is a surface-like feature. At higher frequencies,

the fault looks more like a volume. The seismic attribute study and fault geobody extraction are a proof of concept of the interpretation workflow, besides giving guidelines to the interpreter for fault characterisation. Although we cannot directly relate the seismic data to the fault properties, we can use the seismic attributes (e.g. fault enhancement) to reasonably define the fault architecture, and approximately predict the distribution of rock properties within the fault zone. Our seismic attribute study is complementary to those of Dutzer et al. (2010), Iacopini and Butler (2011) and Iacopini et al. (2012, 2016). The application of the fault-volume extraction workflow to our synthetic models is a proof of concept of the attribute-based methods for identifying faults and fault-related deformations. Dutzer et al. (2010) constrain their interpretation to well-log data, Iacopini and Butler (2011) and Iacopini et al. (2012) to outcrop analogues, and Iacopini et al. (2016) use the correlation of attributes to define clusters and perform an unsupervised seismic facies classification. Our workflow goes further by relating the seismic amplitude to the distribution of elastic rock properties or finite strains within the input fault models, and truly showing that the mapped geobody from seismic is not just an artefact, but a representation of fault damage.

Future work will look at the impact of particle size on the deformation and resolution of the DEM models, as well as the introduction of more complex fault geometries such as faults interacting along strike. In addition, a more accurate study and application of seismic attributes and their correlation (e.g., Iacopini et al., 2016) will help to establish a better interpretation routine for application to real seismic data. We are also working with seismic imaging simulations of outcrop analogues with well-constrained fault related deformation and petrophysical properties (e.g., Rotevatn and Fossen, 2011).

Acknowledgements

This work was funded by the Norwegian Research Council through the project “Seismic Imaging of Fault Zones” (NFR-PET-ROMAKS, project no. 210425/E30). Mechanical modelling was performed using the program cdem3D by Stuart Hardy, finite strain was computed using the program SSPX by Nestor Cardozo and Richard Allmendinger, seismic imaging simulation was performed in SeisRoX (NORSAR), and seismic attribute analysis was carried out using SVI plus (ffA) and a fault damage mapping toolkit developed by ffA. David Iacopini and an anonymous reviewer are thanked for their insight and constructive feedback that helped to improve the quality of the paper.

References

- Aarland, R.K., Skjervén, J., 1998. Fault and Fracture Characteristics of a Major Fault Zone in the Northern North Sea: Analysis of 3D Seismic and Oriented Cores in the Brage Field (Block 31/4). In: Geological Society, 127. Special Publications, London, pp. 209–229.
- Abe, S., van Gent, H., Urai, J.L., 2011. DEM simulation of normal faults in cohesive materials. *Tectonophysics* 512, 12–21.
- Allmendinger, R.W., Cardozo, N., Fisher, D., 2012. *Structural Geology Algorithms: Vectors and Tensors*. Cambridge University Press, 289 pp.
- Bahorich, M., Farmer, S., 1995. 3-D seismic discontinuity for faults and stratigraphic features: the coherence cube. *Lead. Edge* 14, 1053–1058.
- Belheine, N., Plassiard, J.P., Donzé, F.V., Darve, F., Seridi, A., 2009. Numerical simulation of drained triaxial test using 3D discrete element modeling. *Comput. Geotech.* 36, 320–331.
- Botter, C., Cardozo, N., Hardy, S., Lecomte, I., Escalona, A., 2014. From mechanical modeling to seismic imaging of faults: a synthetic workflow to study the impact of faults on seismic. *Mar. Petroleum Geol.* 57, 187–207.
- Cardozo, N., Allmendinger, R.W., 2009. SSPX: a program to compute strain from displacement/velocity data. *Comput. Geosciences* 35, 1343–1357.
- Cardozo, N., Jackson, C.L., Whipp, P.S., 2011. Determining the uniqueness of best-fit trishear models. *J. Struct. Geol.* 33, 1063–1078.
- Carmona, A., Clavera-Gispert, R., Gratacós, O., Hardy, S., 2010. Modelling syntectonic sedimentation: combining a discrete element model of tectonic deformation

- and a process-based sedimentary model in 3D. *Math. Geosci.* 42, 519–534.
- Cheung, G., O'Sullivan, C., 2008. Effective simulation of flexible lateral boundaries in two- and three-dimensional DEM simulations. *Particuology* 6, 483–500.
- Chopra, S., Sudhakar, V., Larsen, G., Leong, H., 2000. Azimuth-based coherence for detecting faults and fractures. *World Oil* 221, 57–62.
- Chopra, S., Marfurt, K.J., 2005. Seismic attributes - a historical perspective. *Geophysics* 70, 350–2850.
- Chopra, S., Marfurt, K., 2007. Seismic attributes for prospect identification and reservoir characterization. *SEG Geophys. Dev. Ser.* 11 (2).
- Chopra, S., Marfurt, K.J., 2009. Detecting stratigraphic features via crossplotting discontinuity attributes and their volume visualization. *Lead. Edge* 28, 1422–1426.
- Cil, M.B., Alshibli, K.A., 2014. 3D analysis of kinematic behavior of granular materials in triaxial testing using DEM with flexible membrane boundary. *Acta Geotech.* 9, 287–298.
- Cohen, I., Coult, N., Vassiliou, A., 2006. Detection and extraction of fault surfaces in 3D seismic data. *Geophysics* 71, P21–P27. <http://dx.doi.org/10.1190/1.2215357>.
- Corfield, S., Sharp, I.R., 2000. Structural style and stratigraphic architecture of fault propagation folding in extensional settings: a seismic example from the Smorbukk area, Halten Terrace, Mid-Norway. *Basin Res.* 12, 329–341.
- Drottning, Å., Branston, M., Lecomte, I., 2009. Value of illumination-consistent modeling in time-lapse seismic analysis. *First Break* 27 (10), 75e83.
- Dutzer, J.F., Basford, H., Purves, S., 2010. Investigating fault-sealing potential through fault relative seismic volume analysis. *Pet. Geol. Conf. Proc.* 7, 509–515.
- Faulkner, D.R., Jackson, C.A.L., Lunn, R.J., Schlische, R.W., Shipton, Z.K., Wibberley, C.A.J., Withjack, M.O., 2010. A review of recent developments concerning the structure, mechanics and fluid flow properties of fault zones. *J. Struct. Geol.* 32, 1557–1575.
- Fehmers, G.C., Höcker, C.F.W., 2003. Fast structural interpretation with structure-oriented filtering. *Geophysics* 68, 1286–1293.
- Ferrill, D.A., Morris, A.P., Sims, D.W., Waiting, D.J., Hasegawa, S., 2005. Development of synthetic layer dip adjacent to normal faults. In: Sorkhabi, R., Tsujii, Y. (Eds.), *Faults, Fluid Flow, and Petroleum Traps*. AAPG Memoir, 85, pp. 125–138.
- Ferrill, D.A., Morris, A.P., Smart, K.J., 2007. Stratigraphic control on extensional fault propagation folding: big Brushy Canyon monocline, Sierra Del carmen, Texas. *Geological Society*, 292. Special Publication, London, pp. 203–217.
- Ferrill, D.A., Morris, A.P., McGinnis, R.N., 2012. Extensional fault-propagation folding in mechanically layered rocks: the case against the frictional drag mechanism. *Tectonophysics* 576–577, 78–85.
- Finch, E., Hardy, S., Gawthorpe, R., 2004. Discrete-element modelling of extensional fault-propagation folding above rigid basement fault blocks. *Basin Res.* 16, 489–506.
- Færseth, R.B., Johnsen, E., Sperrevik, S., 2007. Methodology for risking fault seal capacity: implications of fault zone architecture. *AAPG Bull.* 91, 1231–1246.
- Gersztenkorn, A., Marfurt, K.J., 1999. Eigenstructure-based coherence computations as an aid to 3-D structural and stratigraphic mapping. *Geophysics* 64, 1468–1479.
- Gjøystdal, H., Iversen, E., Lecomte, I., Kaschwich, T., Drottning, Å., Mispel, J., 2007. Improved applicability of ray tracing in seismic acquisition, imaging, and interpretation. *Geophysics* 72, SM261–SM271.
- Gray, G.G., Morgan, J.K., Sanz, P.F., 2014. Overview of continuum and particle dynamics methods for mechanical modeling of contractional geologic structures. *J. Struct. Geol.* 59, 19–36.
- Hale, D., 2013. Methods to compute fault images, extract fault surfaces, and estimate fault throws from 3D seismic images. *Geophysics* 78, O33–O43.
- Han, D., 1986. Effects of Porosity and Clay Content on Acoustic Properties of Sandstones and Unconsolidated Sediments. Stanford University, Department of Geophysics, School of Earth Sciences. PhD Thesis.
- Hardy, S., Finch, E., 2005. Discrete-element modelling of detachment folding. *Basin Res.* 17, 507–520.
- Hardy, S., Finch, E., 2006. Discrete element modelling of the influence of cover strength on basement-involved fault-propagation folding. *Tectonophysics* 415, 225–238.
- Hardy, S., McClay, K., Anton Muñoz, J., 2009. Deformation and fault activity in space and time in high-resolution numerical models of doubly vergent thrust wedges. *Mar. Petroleum Geol.* 26, 232–248.
- Hatchell, P., Bourne, S., 2005. Rocks under strain: strain-induced time-lapse time shifts are observed for depleting reservoirs. *Lead. Edge (Tulsa, OK)* 24, 1222–1225.
- Healy, D., Neilson, J.E., Haines, T.J., Michie, E.A.H., Timms, N.E., Wilson, M.E.J., 2014. An investigation of porosity-velocity relationships in faulted carbonates using outcrop analogues. In: Agar, S.M., Geiger, S. (Eds.), *Fundamental Controls on Fluid Flow in Carbonates*. Geological Society of London, Special Publication, 406, pp. 261–280.
- Henderson, J., 2012. Geological Expression: data driven—interpreter guided approach to seismic interpretation. *First Break* 30, 95–100.
- Hesthammer, J., Fossen, H., 1997. Seismic attribute analysis in structural interpretation of the Gullfaks Field, northern North Sea. *Pet. Geosci.* 3, 13–26.
- Hoek, E., Brown, E.T., 1997. Practical estimates of rock mass strength. *Int. J. Rock Mech. Min. Sci.* 34, 1165–1186.
- Holt, R.M., Fjær, E., Nes, O.M., Stenbråten, J.F., 2008. In: *Strain Sensitivity of Wave Velocities in Sediments and Sedimentary Rocks*, in: 42nd US Rock Mechanics Symposium and 2nd U.S.-Canada Rock Mechanics Symposium. American Rock Mechanics Association, San Francisco, CA.
- Horsrud, P., Sønseth Ø, E.F., Bøe, R., 1998. Mechanical and petrophysical properties of North Sea shales. *Int. J. Rock Mech. Min. Sci.* 35, 1009–1020.
- Höcker, C., Fehmers, G., 2002. Fast structural interpretation with structure-oriented filtering. *Lead. Edge* 21, 238–243.
- Iacopini, D., Butler, R.W.H., 2011. Imaging deformation in submarine thrust belts using seismic attributes. *Earth Planet. Sci. Lett.* 302, 414–422.
- Iacopini, D., Butler, R., Purves, S., 2012. Seismic imaging of thrust faults and structural damage: a visualization workflow for deepwater thrust belts. *First Break* 30, 77–84.
- Iacopini, D., Butler, R.W.H., Purves, S., McArdle, N., De Freslon, N., 2016. Exploring the seismic expression of fault zones in 3D seismic volumes. *J. Struct. Geol.* 89, 54–73.
- Jackson, C.A.L., Kane, K.E., 2012. 3D seismic interpretation techniques: applications to basin analysis, tectonics of sedimentary basins: recent advances. John Wiley and Sons, pp. 95–110.
- Jeanne, P., Guglielmi, Y., Cappa, F., 2012. Multiscale seismic signature of a small fault zone in a carbonate reservoir: relationships between VP imaging, fault zone architecture and cohesion. *Tectonophysics* 554–557, 185–201.
- Kaschwich, T., Gjøystdal, H., Lecomte, I., 2011. Impact of Diffraction on Resolution of PSDM, 73rd European Association of Geoscientists and Engineers Conference and Exhibition 2011: Unconventional Resources and the Role of Technology. Incorporating SPE EUROPEC 2011. Society of Petroleum Engineers, pp. 5420–5424.
- Koledoye, B.A., Aydin, A., May, E., 2003. A new process-based methodology for analysis of shale smear along normal faults in the Niger Delta. *AAPG Bull.* 87, 445–463.
- Kostenko, O.V., Naruk, S.J., Hack, W., Poupon, M., Meyer, H.-J., Mora-Glukstad, M., Anowai, C., Mordi, M., 2008. Structural evaluation of column-height controls at a toe-thrust discovery, deep-water Niger Delta. *AAPG Bull.* 92, 1615–1638.
- Lecomte, I., 2008. Resolution and illumination analyses in PSDM: a ray-based approach. *Lead. Edge (Tulsa, OK)* 27, 650–663.
- Lecomte, I., Kaschwich, T., 2008. Closer to Real Earth in Reservoir Characterization: a 3D Isotropic/Anisotropic PSDM Simulator. 2008 SEG Annual Meeting, 9e14 November. Society of Exploration Geophysicists, Las Vegas, Nevada.
- Lecomte, I., Lavadera, P.L., Anell, I., Buckley, S.J., Schmid, D.W., Heeremans, M., 2015. Ray-based seismic modeling of geologic models: understanding and analyzing seismic images efficiently. *Interpretation* 3, SAC71–SAC89.
- Lecomte, I., Lavadera, P.L., Botter, C., Anell, I., Buckley, S.J., Eide, C.H., Grippa, A., Mascolo, V., Kjøberg, S., 2016. 2(3)D convolution modelling of complex geologic targets beyond – 1D convolution. *First Break* 34, 99–107.
- Long, J.J., Imber, J., 2010. Geometrically coherent continuous deformation in the volume surrounding a seismically imaged normal fault-array. *J. Struct. Geol.* 32, 222–234.
- Long, J.J., Imber, J., 2011. Geological controls on fault relay zone scaling. *J. Struct. Geol.* 33, 1790–1800.
- Lewis, M.M., Jackson, C.A.L., Gawthorpe, R.L., Whipp, P.S., 2015. Early synrift reservoir development on the flanks of extensional forced folds: a seismic-scale outcrop analog from the Hadahid fault system, Suez rift, Egypt. *AAPG Bull.* 99, 985–1012.
- Manzocchi, T., Childs, C., Walsh, J.J., 2010. Faults and fault properties in hydrocarbon flow models. *Geofluids* 10, 94–113.
- Marfurt, K.J., Sheet, R.M., Sharp, J.A., Harper, M.G., 1998. Suppression of the acquisition footprint for seismic sequence attribute mapping. *Geophysics* 63, 1024–1035.
- Marfurt, K.J., Lynn, Kirlin R., Farmer, S., Bahorich, M., 1999. 3D seismic attributes using a semblance-based coherency algorithm. *Geophysics* 63, 1150–1165.
- Marfurt, K.J., Chopra, S., 2007. Seismic attributes for prospect identification and reservoir characterization. *SEG Geophys. Dev.* 11.
- Marfurt, K.J., Alves, T.M., 2015. Pitfalls and limitations in seismic attribute interpretation of tectonic features. *Interpretation* 3 (1), SB5–SB15.
- Mascolo, V., Rusciadelli, G., Lecomte, I., 2015. Synthetic seismic modelling of outcropping carbonate system of the maiella mountain (central Apennines-Italy). In: 77th EAGE Conference and Exhibition 2015.
- Mavko, G., Mukerji, T., Dvorkin, J., 2009. *The Rock Physics Handbook: Tools for Seismic Analysis in Porous Media*, second ed. Cambridge University Press, New York.
- Mora, P., Place, D., 1993. A lattice solid model for the nonlinear dynamics of earthquakes. *Int. J. Mod. Phys. C* 04, 1059–1074.
- Nes, O.-M., Holt, R.M., Fjær, E., 2000. The reliability of core data as input to seismic reservoir monitoring studies. In: SPE European Petroleum Conference. Society of Petroleum Engineers.
- Nygård, R., Gutierrez, M., Bratli, R.K., Høeg, K., 2006. Brittle-ductile transition, shear failure and leakage in shales and mudrocks. *Mar. Petroleum Geol.* 23, 201–212.
- Purves, S., Basford, H., 2011. Visualizing Geological Structure with Subtractive Color Blending. *GCSEPM Extended Abstracts*.
- Rotevatn, A., Fossen, H., 2011. Simulating the effect of subseismic fault tails and process zones in a siliciclastic reservoir analogue: implications for aquifer support and trap definition. *Mar. Petroleum Geol.* 28, 1648–e1662.
- Schöpfer, M.P.J., Childs, C., Walsh, J.J., 2007. Two-dimensional distinct element modeling of the structure and growth of normal faults in multilayer sequences: 1. Model calibration, boundary conditions, and selected results. *J. Geophys. Res. Solid Earth* 112, B10401.
- Schöpfer, M.P.J., Abe, S., Childs, C., Walsh, J.J., 2009. The impact of porosity and crack density on the elasticity, strength and friction of cohesive granular materials: insights from DEM modelling. *Int. J. Rock Mech. Min. Sci.* 46, 250–261.
- Schöpfer, M.P.J., Childs, C., Manzocchi, T., 2013. Three-dimensional failure envelopes

- and the brittle-ductile transition. *J. Geophys. Res. B Solid Earth* 118, 1378–1392.
- Sheriff, R.E., 1991. *Encyclopedic Dictionary of Exploration Geophysics*, 1-56080-018-6.
- Sheriff, R.E., Geldart, L.P., 1995. *Exploration Seismology*. Cambridge university press.
- Sigernes, L.-T., Tjaland, W.E., Morton, A., 2002. Seismic Fault Imaging: SEG Technical Program Expanded Abstracts 21, 516–519.
- Skurtveit, E., Torabi, A., Gabrielsen, R.H., Zoback, M.D., 2013. Experimental investigation of deformation mechanisms during shear-enhanced compaction in poorly lithified sandstone and sand. *J. Geophys. Res. Solid Earth* 118, 4083–4100.
- Smart, K.J., Ferrill, D.A., Morris, A.P., 2009. Impact of interlayer slip on fracture prediction from geomechanical models of fault-related folds. *AAPG Bull.* 93, 1447–1458.
- Townsend, C., Firth, I.R., Westerman, R., Kirkevollen, L., Hårde, M., Andersen, T., 1998. Small seismic-scale fault identification and mapping. In: Jones, G., Fisher, Q.J., Knipe, R.J. (Eds.), *Faulting, Fault Sealing and Fluid Flow in Hydrocarbon Reservoirs*. Geological Society, London, Special Publications, pp. 1–25.
- Weickert, J., 1998. *Anisotropic Diffusion in Image Processing*. B. G. Teubner (Stuttgart), 184pp.
- Withjack, M., Olson, J., Peterson, E., 1990. Experimental models of extensional forced folds (1). *AAPG Bull.* 74, 1038–1054.
- Wood, A.M., Paton, D.A., Collier, R.E.L.L., 2015. The missing complexity in seismically imaged normal faults: what are the implications for geometry and production response?. In: Richards, F.L., Richardson, N.J., Rippington, S.J., Wilson, R.W., Bond, C.E. (Eds.), 2015. *Industrial Structural Geology: Principles, Techniques and Integration*. Geological Society of London, vol. 421. Special Publications, pp. 213–230.
- Zoback, M.D., 2010. *Reservoir Geomechanics*. Cambridge University Press, 461pp.